Physics – Uspekhi **68** (6) 552 – 583 (2025)

CONFERENCES AND SYMPOSIA

PACS numbers: **03.67. – a,** 03.67.Lx, **32.30. – r,** 37.10.De, 37.10.Ty, 42.62.Fi

Quantum computing with trapped ions: principles, achievements, and prospects*

I.V. Zalivako, N.V. Semenin, N.O. Zhadnov, K.P. Galstyan, P.A. Kamenskikh, V.N. Smirnov, A.E. Korolkov, P.L. Sidorov, A.S. Borisenko, Yu.P. Anosov, I.A. Semerikov, K.Yu. Khabarova, N.N. Kolachevsky

DOI: https://doi.org/10.3367/UFNe.2024.12.039884

Contents

1. Introduction **552**
2. Ion trapping **556**
2.1 Ion motion in a Paul trap; 2.2 Types of Paul traps; 2.3 Loading ions
3. Initialization, cooling and readout of the ion states **561**
3.1 Encoding quantum information in ions; 3.2 Initialization of quantum states; 3.3 Ion cooling; 3.4 Readout of the ion states
4. Implementation of quantum gates with trapped ions **565**
4.1 Methods for implementing quantum operations; 4.2 Single-qubit and single-qudit gates; 4.3 Two-qubit gates
5. 50-qubit ytterbium ion quantum computer **573**
5.1 Quantum computer on $^{171}Yb^{+}$ ions; 5.2 Implementation of basic quantum algorithms
6. Conclusions **580**
References **581**

Abstract. Ultracold ions are among the most thriving physical platforms in the field of quantum computing: the long coherence time and the high gate fidelity lead in quantum volume (2^{21}) over other systems, including the superconducting platform (whose maximum demonstrated quantum volume is 2^9). Ion quantum computers have allowed implementing the deepest benchmarking algorithms to date and successfully demonstrating error correction codes, which opens up the prospect of moving from the current era of noisy quantum processors (NISQ) to the next era. In Russia, the field of ion quantum computers began to actively develop with the "Quantum Computing" Roadmap launched in 2020. In this review, we present the basic principles of operation of an ion quantum computer and discuss recent achievements in this area worldwide, along with the main results of our group obtained in implementing the Roadmap.

Keywords: quantum computing, ions, Paul traps, qudits, quantum computers, surface traps

I.V. Zalivako[(1,2)], **N.V. Semenin**[(1,2)], **N.O. Zhadnov**[(1,2)], **K.P. Galstyan**[(1,2)], **P.A. Kamenskikh**[(1,2)], **V.N. Smirnov**[(1,2)], **A.E. Korolkov**[(1,2)], **P.L. Sidorov**[(1,2)], **A.S. Borisenko**[(1,2)], **Yu.P. Anosov**[(1,2)], **I.A. Semerikov**[(1,2)], **K.Yu. Khabarova**[(1,2)], **N.N. Kolachevsky**[(1,2,*)]

[(1)] Lebedev Physical Institute, Russian Academy of Sciences, Leninskii prosp. 53, 119991 Moscow, Russian Federation

[(2)] Russian Quantum Center, Innovation Center Skolkovo, Bol'shoi bul'var 30, str. 1, 121205 Moscow, Russian Federation

E-mail: [(*)] kolachevsky@lebedev.ru

Received 9 December 2024
Uspekhi Fizicheskikh Nauk **195** (6) 585 – 620 (2025)
Translated by S. Alekseev

1. Introduction

Quantum computing is based on the possibility of coherent control of the state of a two-level quantum system (single-qubit operations) and the possibility of entangling two physical quantum systems (two-qubit operations). Naturally, ensuring high-quality computations requires the identity of quantum objects and the highest possible fidelity of operations on them, i.e., controlled transformation of the initial quantum state to the desired one, $|\psi_0\rangle \to |\psi\rangle$. Single atoms and ions are natural quantum objects, which ensures their complete identity in the absence of external perturbations. Quantum information can be recorded in the states of electron levels, and the states can be controlled by well-developed laser or radio-frequency spectroscopy methods. Methods for addressing single atoms and ions, unavailable before the advent of laser cooling and ultrastable lasers, are now well developed and are not a critical limitation on the task of creating a quantum computer. This was noted in the Nobel Prize in Physics awarded to S. Haroche and D. Wineland (2012) for innovative experimental methods that allow measuring and manipulating individual quantum systems [1].

A certain challenge is to ensure a high coherence time of a quantum system and at the same time strong interaction both with the external electromagnetic field and between particles. A high coherence time is required to improve the quality of operations and perform the longest possible algorithmic

* The review is based on a paper presented at the Scientific Session of the General Meeting of the Physical Sciences Division of the Russian Academy of Sciences on 9 December 2024 (see *Phys. Usp.* **68** 551 (2025); *Usp. Fiz. Nauk* **195** 584 (2025)).

sequences. Interactions, in turn, are required to implement quantum operations, and it is desirable that the operations be fast (which means that the interaction must be strong).

A long coherence time implies isolation of a quantum system from external influences and the choice of long-lived internal states, for example, metastable levels. At the same time, a channel for deterministic control of the wave function of the system must be provided, which for single-qubit operations is performed with special pulses of the electromagnetic field (optical or radio-frequency). Decoherence in a given channel can be minimized by using an extremely small number of photons in the corresponding mode when the external field is switched off. The situation is more complicated with two-qubit operations, which require strong interparticle interaction to entangle quantum objects. Ions, unlike atoms, exhibit a strong Coulomb interaction, and the corresponding potential is quantized when low temperatures are reached. If the number of phonons in the Coulomb motional mode is reduced to zero, then almost ideal conditions for performing quantum operations can be provided. By a combination of these factors, ions were chosen as one of the first and very successful platform for building quantum computers.

The basic element of a quantum computer is generally a qudit — a quantum object with $d \geqslant 2$ states. Historically, quantum information theory developed on the basis of classical information, and the consideration was traditionally focused on the binary representation of data and hence on two-level systems, qubits. To align the terminology and definitions with the generally accepted ones, we also mainly deal with the concept of a qubit, except in the sections devoted specifically to multilevel systems. An important feature of quantum computing is the very rapid growth of the dimension of the state space of a quantum system with the number of qubits. Thus, a computational register of N qubits corresponds to a state space of dimension 2^N. The amount of information that can be encoded in a vector in such a space can be illustrated by the fact that its description would require $2 \times 2^N - 1$ real numbers, which for 300 qubits is already approximately 4×10^{90}, a value inaccessible to any classical computer. The computational potential of quantum computers can be effectively used to model other quantum systems and solve optimization, cryptography, quantum chemistry, and many other problems.

The full potential of quantum computers can be realized only when we can fully control the quantum state of the entire register. For this, we must be able to both control the quantum state of each qubit and entangle several qubits with each other with high fidelity. Otherwise, most of the Hilbert space of the register would be inaccessible or the computation result would differ from the expected one. More formally, the requirements for a quantum system to be used as a computer were formulated by DiVincenzo in 1996 [2]: (1) it must be a scalable system with well-defined qubits; (2) it must be possible to prepare qubits in some initial state; (3) the system must have a long coherence time; (4) the system must provide the implementation of a universal full set of quantum operations; (5) it is necessary to be able to measure the states of each qubit. Since the formulation of the basic principles of quantum computing in the 1980s [3–5], the field has come a long way from theoretical concepts to prototypes of real devices [6–10], including those that are commercially available [11–14].

In 1994, Cirac and Zoller [15] proposed using a chain of laser-cooled ions trapped in a linear Paul trap as a physical implementation of a quantum register [16]. Atomic ions in traps naturally represent multilevel quantum systems that are identical to each other within the same isotope and satisfy the DiVincenzo criteria. The use of trapped ions in various areas of physics began with the development of methods for confining charged particles. The radiofrequency ion trap invented in 1953 by Paul [17] has found the widespread application in the field of quantum computing. In 1989, W. Paul and G. Dehmelt (the inventor of another type of ion trap [18]) were awarded the Nobel Prize in Physics.

Particle confinement in Paul traps is achieved by a combination of static and alternating electric fields created by special electrode systems (Fig. 1). A distinctive feature of ion traps is their depth, which can reach several electron volts, equivalent to temperatures of the trapped particles of $\sim 10{,}000$ K. This allows ions to be loaded into traps from heat sources without preliminary cooling, and the lifetime of the trapped particles can reach several months. In addition, Paul traps introduce minimal disturbances into the energy structure of ions and allow the trapped particles to be effectively isolated from external influences. Therefore, such traps do not require a magnetic field for their operation; after laser cooling [19], the ions are localized near the region where the confining electric fields vanish. Considering that such traps are usually placed in vacuum chambers with a residual pressure of less than 10^{-10} mbar, collisions with the background gas can also usually be ignored. These properties allow the third DiVincenzo criterion, a long coherence time, to be met. Thus, the record coherence time among all types of qubits, 1 h, was achieved with the $^{171}Yb^{+}$ ion in a Paul trap [20]. Another advantage of Paul traps is the high degree of localization of individual particles after cooling (from several ten nanometers to a few micrometers). Cooled trapped ions form structures called ion (or ionic Wigner) crystals (Fig. 2). These structures are similar to the crystal lattice of solids and are formed when the kinetic energy of particles becomes less than the energy of Coulomb repulsion between ions and the energy of the interaction with the confining field of the trap. Ion crystals can have linear, two-dimensional, and three-dimensional configurations. The characteristic distance between ions in a crystal is 1–15 μm. Such strong localization and stationarity of the crystal configuration allow an efficient implementation of individual optical addressing of each particle. In addition, the Lamb–Dicke regime [16] is ensured, which occurs when particles are localized in a region smaller than the wavelength of the radiation interacting with them. In this regime, the interaction of ions with radiation occurs predominantly without changing the vibrational state

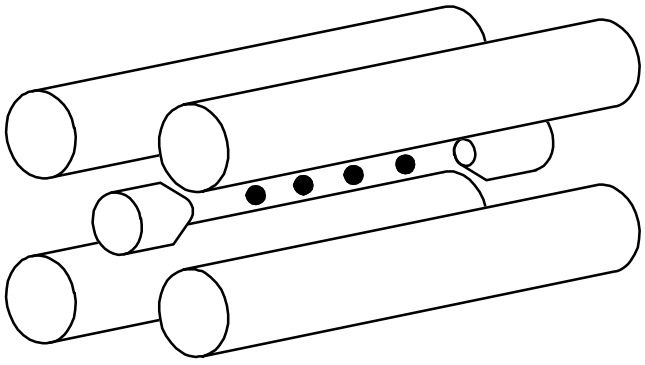

Figure 1. Schematic view of Paul trap. Black dots in middle indicate chain of ions trapped by electrodes.

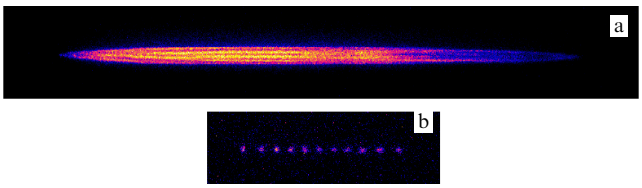

Figure 2. Images of ionic crystals consisting of $^{25}Mg^{+}$. (a) Three-dimensional crystal, (b) linear crystal. Each dot corresponds to a single ion.

of particles, minimizing the effect of particle motion on the fidelity of single-qubit operations. No less important is the fact that, from the mechanical standpoint, ions in a crystal represent a system of coupled harmonic oscillators. This gives rise to collective vibrational degrees of freedom in the ions in the trap, which can be used to entangle the quantum electronic states of the ions with each other.

Thus, laser-cooled ions in a Paul trap satisfy all the DiVincenzo criteria: (1) quantum information can be encoded in the electronic states of ions, the number of trapped ions is limited only by the technical capabilities of controlling their quantum states, and further scaling is realized by quantum interconnections between several individual ion chains [21, 22]; (2) initialization of quantum states is effectively realized by optical pumping methods [23, 24]; (3) record coherence times among all platforms existing today [20] are achieved on ions due to a high degree of isolation from environmental influences; (4) a complete universal set of quantum operations is realized using high-precision single-qubit operations performed using microwave [25, 26] or optical [6, 24] fields, as well as two- [15, 27, 28] or multi-qubit [31, 32] operations using common vibrational modes as the interaction mediator; (5) the states of each ion can be read out with high fidelity using the electron shelving method [6, 16, 24].

As noted above, ion chains in Paul traps were the first proposed physical implementation of a quantum computer [15]. The most important achievement in [15] was the creation of the concept of using collective vibrational modes to perform a two-qubit operation (the Cirac–Zoller gate), namely, the controlled phase operation CPHASE. Just one year after the publication of paper [15] in 1995, Monroe and Wineland, following the approach proposed by Cirac and Zoller, experimentally demonstrated the entanglement of the electronic degrees of freedom of a single beryllium ion in a trap with its vibrational mode, which is a key element of the proposed gate. In 1998, Wineland's group succeeded in implementing the entanglement of two beryllium ions in a trap using a modified Cirac–Zoller method that does not require individual optical addressing of the particles [31], and in 2003, a full-fledged entanglement of two calcium ions with individual addressing was implemented [32], which means that a complete universal set of quantum operations for a two-qubit system was implemented. The main disadvantage of the Cirac–Zoller gate is the need to cool the relevant vibrational mode to the ground state [33]. Because the process of cooling to the ground vibrational state is always performed with some finite accuracy, and also because of the heating of the ion chain after cooling [34–36], this leads to errors in this type of gate.

An alternative to the Cirac–Zoller gate less sensitive to the initial vibrational state was proposed in 1999 by Mölmer and Sörensen [27]. This method (the Mölmer–Sörensen or MS gate) is distinguished by both the relative simplicity of implementation (individual addressing of ions is not required: the operation is performed in a single laser pulse) and a much lower sensitivity to the initial vibrational state of the ions. Although cooling to the ground vibrational state improves the fidelity of this gate, it is not a necessary condition for its implementation. Such a gate was experimentally demonstrated in 2008 in Blatt's group in Innsbruck [37] on a pair of calcium ions. The achieved fidelity of the operation was 99.3(1)%. This type of gate, with minor modifications, is still one of the most widespread in the world. It is also important to note that simultaneous application of this gate, not to two but to a larger number of particles, leads to the generation of maximally entangled Greenberger–Horne–Zeilinger (GHZ) multiparticle states [38].

The third widespread form of two-qubit operation is the geometric gate, first proposed and implemented in 2003 by Wineland's group [39] with a fidelity of 97%. This is a phase gate, and it can be mathematically represented as an MS gate in a different basis. For more details on the types of two-qubit operations on ions, see Section 4.3 of this review.

In addition to the field of quantum computing itself, the development of methods for quantum entanglement of ions in a trap had a significant impact on related research fields, in particular, precision spectroscopy and metrology. Thus, in 2004, Wineland's group proposed using an ensemble of ions in the maximally entangled GHZ state to improve the stability of ion frequency standards [40]. The same group proposed and experimentally demonstrated the most important concepts of sympathetic cooling [41] and quantum-logic spectroscopy [42], which opened up the possibility of studying and using ions with a level structure that prevents their direct cooling and readout for metrological purposes. These techniques have allowed implementing optical frequency standards on aluminum ions with a relative uncertainty of less than 10^{-18} [43], as well as precision spectroscopy of highly charged argon ions [44], which is important for testing fundamental theories, including quantum electrodynamics. For his outstanding discoveries in the field of control of quantum states of single ions, David Wineland was awarded the Nobel Prize in Physics in 2012.

Thus, by 2003–2008, all the necessary experimental primitives for creating a universal ion quantum computer or simulator were demonstrated. This marked the beginning of rapid development of both theoretical and experimental research in this field. In 2005, Monroe's group used a pair of cadmium ions to implement the first full-fledged quantum algorithm, the two-qubit Grover algorithm with a phase oracle [45], with a fidelity of 60(2)%. With more than two ions, experiments were initially focused more on the field of quantum simulations, because many problems in this field can be solved with a lesser degree of control over the quantum system than with a universal computer. For example, in 2011, the first experiments on quantum simulation involving up to 6 particles were carried out [46, 47]. In particular, although the entanglement operations in such a system were implemented only globally, involving all ions simultaneously, the dynamics of an Ising spin chain was simulated. In the same year, a GHZ state of 14 ions was demonstrated [48]. In 2017, this result was improved by Monroe's group, which demonstrated a simulation of the phase transition dynamics in a spin chain with transverse Ising interaction on 53 ions, although this simulation was an analogous one and all operations were

performed only globally [49]. Also in 2018, Blatt's group implemented variational algorithms for simulating H_2 and LiH molecules using up to 4 ions (entanglement operations were again performed only globally, while single-qubit operations were performed with individual addressing). Today, the number of qubits in simulators using Paul traps has reached 512 due to the use of two-dimensional configurations of ion crystals [50].

The development of multiqubit universal computers was initially hindered by the lack of individual addressing of qubits when performing entanglement operations. This was due to the existing types of two-qubit operations that implied the interaction of particles through only one vibrational mode, which imposed the requirement that they be spectrally resolvable. Because axial modes are spectrally more separated from each other, they were used for calculations, which required a nonzero projection of the wave vector of the addressing laser beam onto the trap axis. This, in turn, complicated individual optical addressing. A solution to this problem was proposed by Monroe's group in 2006 [51] and implied a transition to radial motional modes and a generalization of the MS gate to the case of interaction with a large number of modes simultaneously. This approach was experimentally demonstrated in 2014 on ytterbium ions [52], which paved the way to the creation of the first universal quantum computer with 5 qubits on an ion platform in 2016 [53]. The average fidelity of two-qubit operations in the processor was 98%, while a distinctive feature of this computer was its full connectivity, i.e., the ability to implement a two-qubit gate between any pair of qubits in one operation. Full connectivity in ion computers is ensured due to the entanglement via common motional modes that are coupled with all trapped particles simultaneously. The only platform for quantum computing, other than ions, that currently has full connectivity is neutral atoms, where this is achieved by physically moving the atoms toward each other to perform the operation [54]. Besides ions, universal computers existed at that time only on the superconducting platform.

A milestone in the development of ion quantum computing was the creation of the IonQ startup company in 2015 by Christopher Monroe and Youngsang Kim. Major technology companies such as IBM and Google had already joined the development of the superconducting platform at that time, bringing in significant funding and production and engineering resources, but the ion platform had previously been developed exclusively within academia. This step allowed significant technological advances of computer subsystems, increasing their reliability and automation. In 2019, a next-generation computer with 11 qubits on ytterbium ions was presented, utilizing the same technology, with full connectivity and an average fidelity of 99.5% for single-qubit operations and 97.5% for two-qubit operations. Cloud access to this system was also provided on a commercial basis. In 2022, the same company released the 25-qubit Aria processor with single-qubit and two-qubit operation fidelity of 99.94% and 99.4%. This system implemented cryogenic cooling of the vacuum chamber to increase the lifetime of the ion chain and reduce particle heating. Soon, the IonQ Forte computer was presented with a new optical addressing system based on ultraviolet acousto-optic deflectors (AODs) and next-generation surface traps, where the number of qubits was increased to 36, and the fidelities of single-qubit and two-qubit operations were respectively increased to 99.98% and 99.6%.

The next step in the development of ion quantum computers was made by the large American company Honeywell, which presented its prototype of a computer based on ytterbium ions in 2020 [21]. This prototype combined almost all the advanced solutions available at that time, including multisection surface chip traps, a cryogenic vacuum chamber, specialized electronics, powerful and highly-stable ultraviolet laser sources, reconfiguration of ion crystals, and sympathetic cooling. An important feature distinguishing the prototype from those considered above was that, here, the ions were held not in one common zone of the trap but in different zones. The design of the trap and electronics allowed each ion to be moved individually, brought closer together whenever necessary to perform two-qubit operations, to be separated, to be swapped, and much more. This concept was initially proposed back in 1998 in Wineland's group [55, 56] and was called a quantum charge coupled device (QCCD). Such approaches were studied in most detail at the Sandia National Laboratory in California [57–61], the results of which were subsequently used by Honeywell. The presented prototype had 4 qubits with full connectivity using ion shuttling, with the fidelity of the respective single-qubit and two-qubit operations being 99.99% and 99.2%. Also, the possibility of an mid-circuit measurement of the ion subregister was demonstrated using the QCCD technology, which is an important element for a number of algorithms, including error correction. In addition, Honeywell adopted the quantum volume metric [62], originally proposed by IBM for superconducting processors.

Quantum volume is a metric that incorporates such processor characteristics as the fidelity of single-qubit and two-qubit operations, the number of qubits, their connectivity, and the ratio of the operation time to the coherence time. The quantum volume of a system is the largest number 2^N, such that the average probability of obtaining 'heavy output values' [63] after running circuits of a special type on a subregister of N qubits is more than 2/3. ''Heavy output values'' are those measured states of a quantum register whose theoretical probability of being obtained on an ideal noiseless quantum processor is above the median. The circuits for characterizing the quantum volume are shown in Fig. 3 and consist of N layers. In each layer, all N qubits are randomly divided into pairs, and randomly chosen Haar-uniform from SU(4) two-qubit operations are performed on each pair. It turns out that such a metric is one of the most

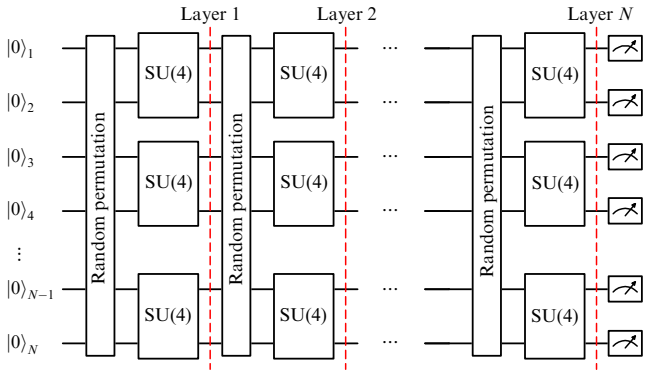

Figure 3. Form of quantum circuits used to characterize quantum volume. Each SU(4) gate in the figure is a random, Haar-uniform chosen from SU(4) two-qubit operation.

rigorous integral metrics used today and can be interpreted as the dimension of the quantum subregister that can be effectively used for sufficiently complex quantum algorithms.

In their first prototype quantum computer, Honeywell demonstrated the largest quantum volume of 2^4 achievable in a register of that size. Honeywell's quantum computing division then spun off into a separate company, Quantinuum, and merged with another quantum algorithm developer. Quantinuum continued rapidly developing ion technology, demonstrating impressive progress in quantum volume [64]. The first-generation H1-1 and H1-2 processors were similar to the first generation of Quantinuum's, featuring a linear architecture, full ion shuttling connectivity, up to 20 particles, 5 qubit zones for simultaneous two-qubit operations, the capacity for mid-circuit measurement, and support for parameterizable native gates. As a result, the H1 system demonstrated the highest two-qubit gate fidelity of 99.9% and the highest single-qubit fidelity, 99.998%, among universal computers commercially available at the time. The quantum volume of this system was 2^{20} (the maximum for this register size). The next generation of the H2 processor [6], introduced in 2023, surpasses the H1 in terms of the number of qubits (56), the speed of ion movement (due to the replacement of the linear architecture with a ring one), the cooling speed, and the quantum volume of 2^{21}, which is a world record now. For comparison, the best result achieved by its closest competitor, the IBM Falcon R10 Prague superconducting processor, was 2^9 in 2022, which means less than half as many 'useful' qubits. We note, however, that many other companies use other metrics, such as algorithmic qubits (IonQ) [10] or characterize their systems only on a component-by-component basis (Google, Harvard University), which complicates direct comparisons.

In Russia, the development of quantum computing on an ion platform began in 2020 within a framework of the leading research center 'Quantum computing' (funded by RVC). The goal was to create a 5-qubit ion computer and connect it to the cloud platform. The project was followed up by the Roadmap for Quantum Computing (2020–2024, Rosatom), which made it possible to demonstrate a 50-qubit ytterbium ion computer and a number of algorithms implemented on this platform by the end of 2024. In Section 5.1, we present the main results obtained during the implementation of the Roadmap. Also, as part of the Roadmap, a laboratory was created at the Russian Quantum Center, with the task to build a quantum computer on calcium ions [7]. A number of important experimental and theoretical results were obtained [29, 65–73], and world-class fidelity values for single- and two-qubit operations were achieved.

Further in the review, we describe the main approaches and methods used in building ion quantum computers, describe the implementation of some algorithms performed by our group, and present the characteristics of a 50-qubit ytterbium ion computer created within the Roadmap framework.

2. Ion trapping

2.1 Ion motion in a Paul trap

Let us discuss the main aspects of the confinement of single ions and ion chains in a linear Paul trap.

2.1.1 Classical consideration, single ion. In a Paul trap, the radio-frequency potential is close to the quadrupole one in the trapping region:

$$\Phi(x,y,z,t) = \frac{U}{2}\left(\alpha x^2 + \beta y^2 + \gamma z^2\right) + \frac{\tilde{U}}{2}\left(\alpha' x^2 + \beta' y^2 + \gamma' z^2\right)\cos\left(\omega_{\mathrm{rf}} t\right). \quad (1)$$

Here, the first term is the static part, the second is the radio frequency part (with the frequency ω_{rf} of the order of 10–20 MHz). This expression is written in a quasistatic approximation, i.e., it is assumed that, at each moment of time, the potential has this coordinate dependence in the entire volume under consideration. This approximation is valid if the wavelength of the radio frequency field of the trap is much larger than characteristic dimensions of the trap, which is always the case in practice. In the same approximation, the wave equation for the field is written as the Laplace equation

$$\Delta\Phi = 0\,, \quad (2)$$

which holds for any U, $\tilde{U}$, and ω_{rf} if

$$\alpha + \beta + \gamma = 0, \quad \alpha' + \beta' + \gamma' = 0\,. \quad (3)$$

To perform quantum computation on ions, a configuration is usually chosen such that

$$-\alpha = -\beta = \frac{\gamma}{2} > 0\,, \quad \alpha' = -\beta'\,, \quad \gamma' = 0\,. \quad (4)$$

The physical meaning of this configuration amounts to the presence of a preferred axis (the z-axis in this case), such that the confinement along it is purely static. The ions that make up the quantum register subsequently align linearly along the same axis. The motion of an ion along the z-axis is harmonic, with the oscillation frequency

$$\omega_z = \sqrt{\frac{\gamma e U}{m}}\,, \quad (5)$$

where m is the mass of the ion and e is its charge (positive here and hereafter). The radial motion equation takes the form (for the x-axis)

$$\frac{\mathrm{d}^2 x}{\mathrm{d}\tau^2} - \left(a - 2q\,\cos\left(2\tau\right)\right)x = 0\,, \quad (6)$$

where the parameters a, q, and τ in the notation of Eqn (1) are

$$\tau = \frac{\omega_{\mathrm{rf}} t}{2}\,, \quad a = \frac{4eU\alpha}{m\omega_{\mathrm{rf}}^2}\,, \quad q = \frac{2e\tilde{U}\alpha'}{m\omega_{\mathrm{rf}}^2}\,. \quad (7)$$

The equation of motion along the y-axis is written similarly.

A differential equation of type (6) is called the *Mathieu equation* [16]. The solutions of this equation are, accordingly, the Mathieu functions. The stability of the trajectories described by the Mathieu functions is determined by the parameters a and q. In particular, Floquet's theorem [74] asserts the existence of periodic solutions of the Mathieu equation for pairs (a,q) falling into the so-called *stability region* [16]. When the stability condition is satisfied, the Mathieu functions are expanded in a Fourier series as

$$x(\tau) = A\exp\left(\mathrm{i}b\tau\right)\sum_{n=-\infty}^{\infty} C_{2n}\exp\left(\mathrm{i}2n\tau\right) + B\exp\left(-\mathrm{i}b\tau\right)\sum_{n=-\infty}^{\infty} C_{2n}\exp\left(-\mathrm{i}2n\tau\right), \quad (8)$$

where A and B are arbitrary constants that define the initial conditions, and the coefficients b and C_{2n} are related to each other by a set of certain recurrence relations [16] that depend on a and q. The most obvious form of the ion motion is in the case $(|a|, q^2) \ll 1$. It can then be shown [16] that $b \approx \sqrt{q^2/2 - a}$, and the coefficients $C_{\pm 2n}$ can be neglected for $n \geqslant 2$. In this formulation, the law of ion motion is ($A = B$)

$$x(t) = 2AC_0 \cos\left(\frac{b\omega_{\rm rf}}{2}\, t\right)\left[1 - \frac{q}{2}\cos\left(\omega_{\rm rf}\, t\right)\right]. \tag{9}$$

From (9), we can understand the general nature of ion oscillations in the trap along the radiofrequency confinement axis. An ion performs harmonic motion with a low frequency compared with the frequency of the confining field, $b\omega_{\rm rf}/2 \ll \omega_{\rm rf}$, on which a high-frequency low-amplitude modulation proportional to q ($q^2 \ll 1$) is superimposed. These small fast oscillations are called *micromotion*, and the above-mentioned slow oscillations are called *secular motion*. The frequency of such motion is called the *secular frequency*:

$$\omega_r = \frac{b\omega_{\rm rf}}{2} \approx \frac{\omega_{\rm rf}\sqrt{q^2/2 - a}}{2}. \tag{10}$$

2.1.2 Ion chain oscillations, normal modes. Technically, the simplest implementation of a quantum register of ion qubits is a continuous array of ions placed in a common linear Paul trap (e.g., Fig. 1). Such a configuration has the advantage that the trap axis corresponds to zero amplitude of the radiofrequency field. This, in turn, means that the micromotion in this location is minimal. Because micromotion leads to the heating of ions [75], which degrades the fidelity of quantum operations, linear chains are a priority choice for a quantum register.

We note that the ions do align along the trap axis only if the axial frequency ω_z in (5) is much smaller than the radial secular frequency ω_r in (10). There is an approximate relation between the ratio ω_r/ω_z required for linearity and the number of ions in the chain N [76]:

$$\frac{\omega_r}{\omega_z} > \frac{0.77N}{\sqrt{\log N}}. \tag{11}$$

Thus, as the number of ions in the trap increases, a fixed radial frequency requires increasingly weaker axial confinement.

Small oscillations of the system about the equilibrium position are a linear combination of *normal modes* characterized by their frequencies and their amplitude vectors. The search for these characteristics reduces to the problem of finding the eigenvectors and eigenvalues of the matrix of second derivatives of the potential V evaluated at the equilibrium positions $z_i^{(0)}$. It can be shown that the matrices

$$\left(\frac{\partial^2 V}{\partial z_i\, \partial z_j}\right)_{\{z_i^{(0)}\}}, \quad \left(\frac{\partial^2 V}{\partial x_i\, \partial x_j}\right)_{\{z_i^{(0)}\}} \tag{12}$$

for calculating the respective axial and radial modes are linearly related to each other [77]. This means that, first, the ratios between the oscillation amplitudes of different ions for the corresponding radial and axial modes coincide (Fig. 4), and second, the frequencies of such modes are uniquely expressed through each other,

$$2(\omega_r^2 - \omega_{r,k}^2) = \omega_{z,k}^2 - \omega_z^2, \tag{13}$$

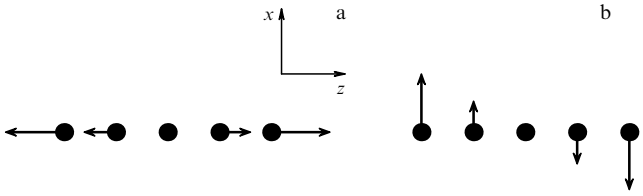

Figure 4. Example of corresponding normal modes: (a) axial and (b) radial. Arrows indicate amplitude and direction of oscillations of corresponding ion in the chain.

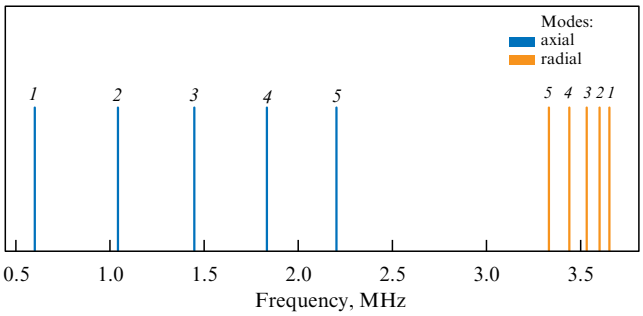

Figure 5. Spectrum of oscillation modes for chain of 5 ions. Frequency values are $\omega_z = 0.6$ MHz and $\omega_r = 3.65$ MHz. Numbers above lines indicate mode numbers.

where $\omega_{r,k}, \omega_{z,k}$ are the respective frequencies of the radial and axial kth mode, ($\omega_{r,1} = \omega_r$, $\omega_{z,1} = \omega_z$). The axial frequencies increase with increasing k, and therefore, in accordance with the formula above, the radial frequencies decrease, i.e., are bounded from above by the frequency ω_r. Moreover, due to the large difference between the axial and radial frequencies, the spectral distance between neighboring radial modes is noticeably smaller than between axial modes. An example of typical axial and radial spectra in a trap with five ions is shown in Fig. 5.

2.1.3 Ion-field interaction. The interaction of the field with an ion can be represented by the Hamiltonian

$$\hat{H}_{\rm I} = \hbar\Omega(|0\rangle\langle 1| + |1\rangle\langle 0|)\cos\left(\mathbf{k}\hat{\mathbf{r}} - \omega t + \phi\right), \tag{14}$$

where Ω is the Rabi frequency, $\mathbf{k}$ is the wave vector of the field, $\hat{\mathbf{r}}$ is the radius vector of the ion, ϕ is the phase of the field, and ω is the frequency of the field. The Rabi frequency Ω depends on the transition type (electric, quadrupole, magnetic dipole, etc.), the field amplitude and polarization, and the beam direction [78].

After switching into the interaction picture, the Hamiltonian can be written as

$$\hat{H}_{\rm int} = \frac{\hbar\Omega}{2}\,\sigma_+ \exp\left[{\rm i}\sum_l \eta_l\left(\hat{a}_l \exp\left(-{\rm i}\omega_l t\right) + \hat{a}_l^{\dagger}\exp\left({\rm i}\omega_l t\right)\right)\right] \times \exp\left({\rm i}(\phi - \Delta t)\right) + {\rm h.c.}, \tag{15}$$

where h.c. denotes Hermitian conjugation and Δ is the detuning of the field frequency from the transition frequency. The operators $\sigma_+ = |1\rangle\langle 0|$ and $\sigma_- = |0\rangle\langle 1|$ act in the ion's internal electronic level space. The coefficient η_l is called the *Lamb–Dicke parameter* and is calculated as

$$\eta_l = kb_{l,j}\sqrt{\frac{\hbar}{2m\omega_l}}, \tag{16}$$

where ω_l is the vibrational frequency of the lth normal mode and $b_{l,j}$ is the normalized amplitude of ion oscillations in this mode (j is its number in the chain).

Let us consider the case of resonant interaction $\Delta = 0$. Then, in the Lamb–Dicke regime ($\eta_l \ll 1$), the interaction Hamiltonian can be reduced to the form

$$\hat{H}_{\text{int}} = \frac{\hbar\Omega}{2}\left(\sigma_+ \exp(\mathrm{i}\phi) + \sigma_- \exp(-\mathrm{i}\phi)\right). \quad (17)$$

This Hamiltonian describes resonant Rabi oscillations and is used in Section 4.2.

2.2 Types of Paul traps

2.2.1 Bulk traps. Strictly speaking, when implementing the alternating electric field potential described in Section 2.2.1, the equipotential lines in the plane perpendicular to the trap axis are hyperbolas. Thus, electrodes with a hyperbolic profile can be used to create such a field, which, however, is rarely implemented in practice.

There are two widely used electrode configurations that provide radial confinement in Paul traps: rod-shaped electrodes (Fig. 6a) and blade-shaped electrodes (Fig. 6c). From the standpoint of providing the necessary radial secular frequencies in the trap, the ratio between the amplitude V_0 of the alternating voltage applied to the electrodes and the distance from the geometric center of the trap to the electrode r_0 is important. An increase in r_0, maintaining the secular frequency at the same level, requires increasing the voltage amplitude on the electrodes, which makes smaller traps preferable. The confinement along the trap axis is achieved either by means of end electrodes (shown in green in Fig. 6a, c), to which a constant potential is applied, or by segmenting the radial confinement electrodes and shifting the potential of the end electrodes relative to the central segment (Fig. 6b, d).

Another important factor for quantum computing is the fidelity of readout of the ion states in the trap, which dictates the need to ensure good optical access to the ions. Due to the foregoing, the configuration based on blade-shaped electrodes turns out to be more successful at the same size r_0. In such traps, the confinement of large ion chains, the implementation of one-qubit and two-qubit gates [32, 79], and the preparation of entangled multiparticle states [48] have been demonstrated.

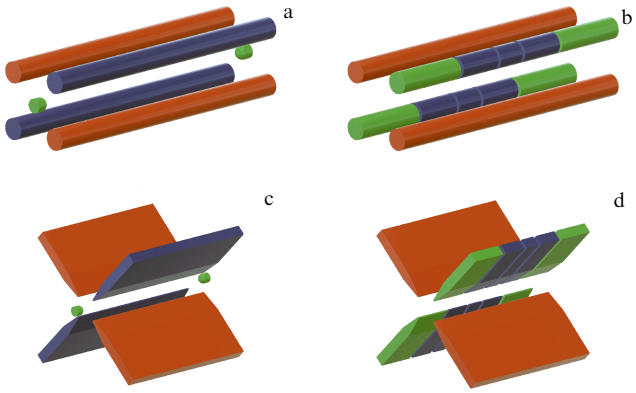

Figure 6. Basic implementations of Paul traps: (a) simple and (b) segmented trap with round electrodes, (c) simple and (d) segmented trap with blade-shaped electrodes. Red electrodes are supplied with alternating voltage, blue electrodes, with constant potential, which makes part of confining potential in radial direction, and green electrodes, with constant potential for longitudinal confinement of ions in the trap.

For more precise control over the position of ions on the traps axis, segmentation of the trap electrodes can be used (Fig. 6b). This approach allows more precise control of the distance between ions, as well as their movement along the trap axis, to bring the ions closer or separate them (Fig. 6d). Lack of necessity for end electrodes also improves optical access to the ions along the axis.

In terms of the materials and technologies used in manufacturing trap parts, including electrodes, a high accuracy of the trap geometry must be ensured to minimize the heating rate of the captured ions. It is possible to manufacture electrodes from metals such as copper, stainless steel, and molybdenum, as well as from dielectrics (for example, alumina ceramics) with subsequent gold coating. Manufacturing of metal trap parts by electrical discharge machining is typically used, ensuring micron-level accuracy of the geometry of the final parts.

2.2.2 Surface traps. The creation of a quantum computer capable of solving useful practical problems requires a multiple increase in the number of ion qubits used. Bulk traps allow confining linear arrays of more than 100 ions [80], but the efficiency of performing operations on such large chains is limited. First, upon increasing the number of ions N in the chain, the speed of two-qubit gates $R_{\text{gate}} \approx \eta \times \Omega$ usually decreases, where $\eta = \sqrt{\hbar k^2/2m_0 N\omega}$ is the Lamb–Dicke parameter, m_0 is the mass of one ion, ω is the frequency of the motional mode, and Ω is the Rabi frequency [78, 81]. Such gates are implemented by exciting the common motional mode by transferring momentum from laser radiation to the ion. In long chains, the coefficient reflecting the participation of the motion of an individual ion in the collective mode is smaller, which slows down the laser excitation of the chain vibrations [78]. The longer the operation is performed, the more decoherence processes (heating of vibrational modes and field fluctuations) diminish the two-qubit gate fidelity.

Second, with increasing chain length, the distances between ions, especially in the central region, decrease to several micrometers (≈ 4 μm in [80]). In such an arrangement, laser beams for individual ion addressing affect not only the target ion but also its neighbors, violating their quantum state.

Third, all bulk traps are manufactured using various types of mechanical processing methods and are quite large devices (several centimeters in size). Although such traps effectively perform their functions, their design and manufacturing methods are poorly suited for creating compact devices with a distributed structure, which are necessary for scaling quantum computing.

The QCCD architecture of a large-scale ion-qubit quantum computer was proposed in 2002 [56]. It is a set of connected ion traps, between which individual ions or chains of ions can be moved using electric fields created by additional control DC electrodes. The convenience of such a system is that the ion quantum processor can be divided into several functional zones: the interaction zone, where the ions are located in a single chain and interact with each other and with laser radiation, the memory zone, where qubits that are not used at a certain stage of the quantum algorithm are located, and the loading zone, where the ion array is replenished. The ions must be moved among these zones during the execution of the quantum algorithm.

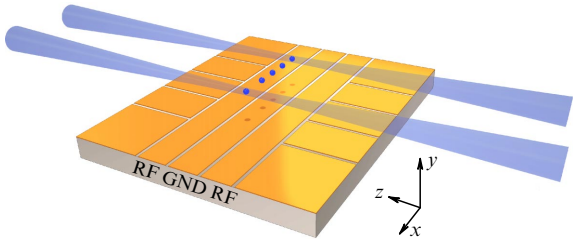

Figure 7. Structure of electrodes of surface Paul trap. Confinement of ions in y and z directions is provided by radiofrequency potential applied to RF electrodes; central electrode is grounded (GND), and side segmented electrodes provide confinement and movement of ions along x-axis. Laser beams are usually directed parallel to trap plane.

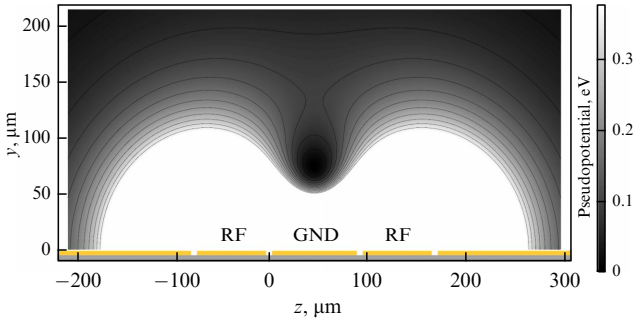

Figure 8. Illustration of pseudopotential of surface Paul trap formed by system of five electrodes. Trap electrodes are shown at bottom. Pseudopotential function is calculated according to [85] where the radiofrequency voltage has an amplitude of 100 V. Depth of confinement potential is 94 meV, confinement height above trap surface is 75 μm.

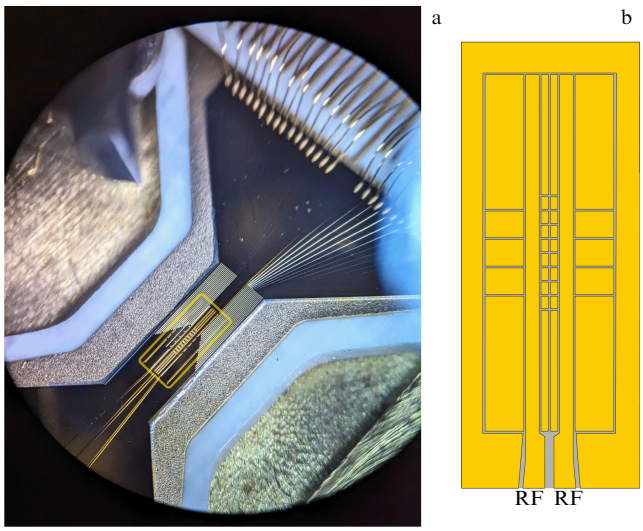

Figure 9. Surface Paul trap on a microchip developed at Lebedev Physical Institute and manufactured at Moscow Institute of Electronic Technology. Structure is grown on silicon substrate and has three layers of gold separated by layers of silicon nitride. Area of trap highlighted in photograph (a) is shown schematically in Fig. b. Trap has two RF electrodes, 20 internal, and 10 external DC electrodes.

Initially, QCCD was proposed to be implemented based on Paul traps in a classical four-electrode configuration, but with flat RF and DC electrodes arranged in three layers (the upper and lower ones form the trap potential, and the middle one creates control electric fields for ion positioning). The basic step for implementing the proposed approach — moving ions between neighboring traps — was demonstrated by the same group [82].

In 2005–2006, an alternative design of a radiofrequency Paul ion trap was proposed [83] and demonstrated experimentally [84], in which the field is created by electrodes located in the same plane. The most widespread configuration, consisting of five planar electrodes, is obtained by directly projecting four electrodes of a volume trap onto the plane. In this scheme, the outer and central electrodes are grounded, and the radiofrequency voltage is applied to the pair of remaining electrodes (Fig. 7). The minimum of the pseudopotential is located above the central electrode, and the trap axis is directed along the electrodes (Fig. 8). Several segments of the outer electrodes are used for axial confinement of ions: for example, applying a positive voltage to the corner electrodes (see Fig. 7) allows forming a potential well along the trap axis with a minimum at its center. The high precision and availability of photolithographic methods for creating such traps, wide optical access to ions, and the possibility of constructing an arbitrary surface structure of electrodes are ideal for implementing the QCCD scheme.

In surface traps, ion movement occurs due to a change in the shape of the electric potential above the trap plane. By smoothly switching the voltage on the DC electrodes, the potential minima are moved along the trap axis together with the ions [86, 87]. The movement of ions in a two-dimensional plane above the surface of a chip trap allows manipulating several ion chains on a single chip as a single quantum register: connecting and separating chains, exchanging ions between them, and performing quantum operations on any pair of qubits. The SWAP logical operation, for example, can be implemented by physically swapping neighboring ions [88].

Compared to bulk traps, planar traps are distinguished by an approximately order of magnitude smaller depth of the confining pseudopotential at an equal amplitude of the radiofrequency voltage, as well as by the asymmetry of the potential well in the radial plane. The typical distance d from the ion to the chip surface is 50–100 μm, which can significantly limit the numerical aperture (NA) of the Gaussian laser beam used for ion addressing. Traditionally, microchips with ion traps are manufactured in the form of a bow tie, with the trap zone located in the isthmus with a width of about 1 mm (Fig. 9). In this configuration, the NA is approximately 0.2 for beams propagating parallel to the trap plane and perpendicular to the isthmus, which suffices for using beams with a waist diameter of less than 2 μm for individual ion addressing. The amplitude of the radiofrequency voltage supplied to the surface trap is limited by the breakdown voltage between closely spaced electrodes ($\lesssim$300–400 V), but it is comparable to the maximum voltages used in volumetric traps.

The effects of ion heating in surface traps are stronger due to their proximity to the electrodes. Heating of ion vibrations is caused by fluctuations of the electric field at the confinement point. The main sources of such fluctuations are the instability of the electrode surface potentials (patch potentials) and thermal noise (Johnson–Nyquist noise), which increase with decreasing distance d to the electrodes proportionally to $1/d^4$ and $1/d^2$, respectively [89]. The heating rate can be reduced by using optimal materials for the surface electrodes, cleaning the surface, and using cryogenic temperatures [90]. The lowest heating rates recorded in planar ion traps are several ten phonons per second.

The design of microchips with surface ion traps is becoming increasingly complex, and many devices required for quantum computing and simulations are gradually being integrated directly onto the chip. These include optical waveguides, photon detectors, and electrical components such as inductors and radio frequency filters [91]. Modern ion chips can include several hundred programmable electrodes [6], with traps arranged in several rows and ion chains moving between them via X-, Y-, and T-shaped connections [92]. For ease of addressing, some traps have a slot cut along the axis to the full depth of the chip, allowing laser beams to pass through the trap and precisely affect the trapped ions [93]. Often, such microchips with ion traps are placed in standard CPGA cases used in computer processors.

In recent years, research has begun in Russia in the field of development and application of surface ion traps. Research groups from the Lebedev Physical Institute of the Russian Academy of Sciences (LPI) [94] and the Russian Quantum Center (RQC) [95] are working on creating ion-trap microchips for quantum computers. A group from the Skolkovo Institute of Science and Technology [96] is developing a compact optical clock using a planar trap. An example of a chip trap developed at the LPI and MIET is shown in Fig. 9.

2.3 Loading ions

Any quantum computing experiment begins with loading one or more ions into a radio frequency trap. Currently, many laboratories working with the ion computing platform are moving to the active use of planar technologies [6, 21, 97]. In this regard, ion processors are becoming smaller, and the experimental challenges caused by the loading procedure are becoming increasingly critical for the implementation of high-quality quantum computing.

Typically, the process of loading ions into a trap consists of three main stages: creating a flux of neutral atoms, the ionization procedure, and the ion trapping procedure. The two most common methods for obtaining a flux of neutral atoms are using an atomic oven [98] and using pulsed laser ablation [99]. Setups for implementing these methods are shown in Fig. 10. Also, in more complex experiments, magneto-optical traps are sometimes used, in which neutral atoms can be trapped and localized at a point in space required for the experiment.

Historically, the first method classically used for creating an atomic flux employs an oven, which produces a directed thermal beam of neutral atoms by heating an atomic source inside a vacuum chamber. The oven is a container with a sample of the substance, equipped with a resistive heater. When the heater is turned on, the oven, due to the effusion process, creates a beam of neutral atoms, which is directed such that it passes through the trapping area of the ion trap. However, this method has a number of disadvantages. The flow of atoms created by an atomic oven is continuous and cannot be quickly turned off, which inevitably leads to an excess of evaporated atoms, extremely undesirable in the experiment. With such a loading process, atoms from the beam can be deposited on the electrodes of the trap or dielectric surfaces, leading to its local contamination. It has been shown that the accumulation of contaminants on the trap electrodes significantly increases the heating rate of the trapped ions over time [100, 101]. Also, the combination of ion traps with optical resonators [102] places stringent requirements on the loading process, because any contamination of the mirror surfaces degrades the quality of the resonator.

With an atomic oven, the ionization of neutral atoms is usually carried out either by electron impact or by the resonance photoionization method. The electron impact method is performed using an electron gun. Electrons are accelerated and collimated such that the resulting electron beam intersects with the atomic beam in the trapping area. The potentials of the accelerating electrodes must also provide an electron energy sufficient for a high impact ionization cross section. However, this method is nonselective: atoms of any elements and isotopes that are at the intersection of the electron beam and the trapping area are subject to the ionization process. The ionization process also affects the background gas atoms that remain after the vacuum chamber has been evacuated. Therefore, the resonance photoionization method is preferable: it ensures selectivity of the isotopes loaded into the trap and therefore has a higher efficiency compared to electron impact. The loading efficiency using the photoionization method is up to five orders of magnitude greater [103, 104] than that of the electron impact method. Therefore, a much smaller flux of neutral atoms is required for ionization, which reduces contamination of the trap electrodes [105].

The method of creating an atomic flux by means of pulsed laser ablation resolves some of the problems that arise when using atomic ovens. The laser ablation method uses high-energy laser pulses that act on a target made of a selected material and heat a strictly localized area to high temperatures. This creates beams of atoms that leave the target surface in response to each laser pulse. The evaporation of atoms by ablation can be maintained for as long as it takes to obtain the desired number of trapped ions. Thus, after

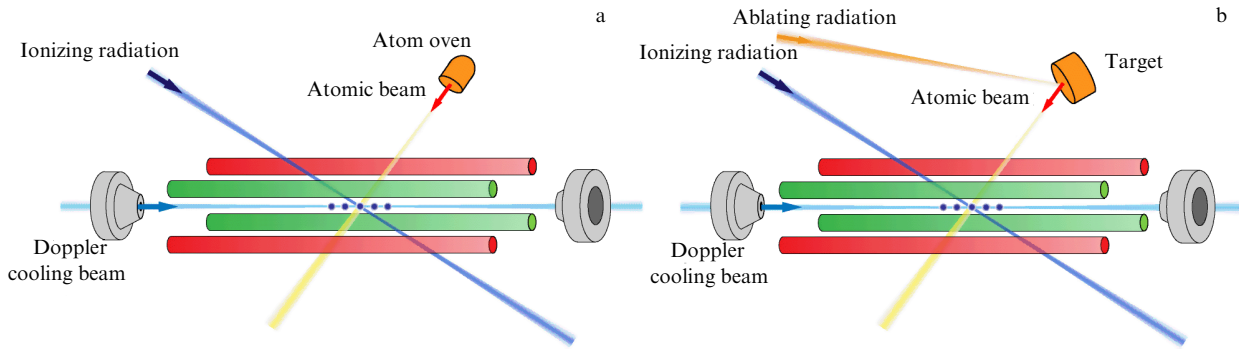

Figure 10. Main methods for loading ions into a radio frequency trap: (a) by creating atomic flux using an oven, (b) by creating atomic flux using laser ablation in combination with resonant photoionization method.

loading the required number of ions, the ablation process can be stopped immediately. At the same time, due to the high temperatures of the ablated atoms, the loading can be less efficient compared to using an atom oven for shallow traps. However, loading of a planar trap with a trapping depth of only 40 meV was demonstrated in [99]. Together with the resonance photoionization method, ions can be loaded into the trap isotopically selectively.

Using magneto-optical traps, it is possible to localize neutral atoms in the central region of the ion trap, and, after photoionization, catch the ionized atoms directly into the ion trap [106]. The advantage of this approach is that ion loading is much more efficient if the ion trap has a small trapping potential. For example, the loading rate of the ion trap in [107] exceeds the rate achieved by photoionization (ionization by electron impact) of an atomic beam by four (six) orders of magnitude. In this paper, it was demonstrated that shallow traps (0.13 eV) are easily loaded using this technique.

3. Initialization, cooling and readout of the ion states

3.1 Encoding quantum information in ions

Information in ion qubits is usually encoded in the internal states of the particle, and the generalized vibrational degrees of freedom of the ion chain act as a mediator of the interaction between them.

To implement computations, the ion must have a suitable energy structure. In particular, it must typically have a pair of metastable levels that could be used as states encoding the qubit, as well as a cyclic transition for cooling, initialization, and readout. Most often, the most convenient structures are those of ions of group II elements (for example, Be^+, Mg^+, Ca^+) or some lanthanides and actinides (Yb^+, Lu^+, Th^+). This is due to the presence of one electron in their valence shell, which makes them hydrogen-like.

There are several types of ion qubits, differing in the types of transitions between qubit states (Fig. 11). The first of them is an optical qubit. There, the qubit levels are connected by a narrow optical transition (usually E2) with a frequency of several hundred THz, which explains its name. Usually, one of its levels is the ground electron state of the ion, and the other is some metastable state, for example, one from the D-level, which has a lifetime from several ten milliseconds to tens of seconds for many particles under consideration. The second frequently used type is a microwave qubit. It is typically implemented using the transition between two states of the hyperfine structure of the ion, with the frequency in the range from a few to ten GHz, which is why such qubits are often called hyperfine. The third type is a Zeeman (or radio frequency) qubit qubits. It is formed by several Zeeman sublevels of a certain spectral term, and its frequency is from several units to hundreds of MHz.

Each of the qubit types has its own advantages and disadvantages. The optical-type qubit allows easy individual addressing of each ion in the register using a single, narrowly focused laser beam. The disadvantage of the optical qubit is the limited lifetime of the excited state. The advantage of the Zeeman qubit is that the levels are sufficiently close and can be controlled by simple radio frequency sources and antennas, but the coherence time is short due to the strong sensitivity to the magnetic field, and it is difficult to read and address qubits of this type individually. One of the most common qubit types is the microwave qubit [6, 37, 108]. Its advantage is a long coherence time, which can be more than a minute [24] or more than an hour when using active dephasing suppression (dynamical decoupling) methods [20]. However, the microwave qubit also requires more complex approaches to ensure individual addressing compared to the optical one. Operations with it are performed using Raman transitions [109] or a microwave field [110]. For more information on the methods for controlling different types of qubits, see Section 4.

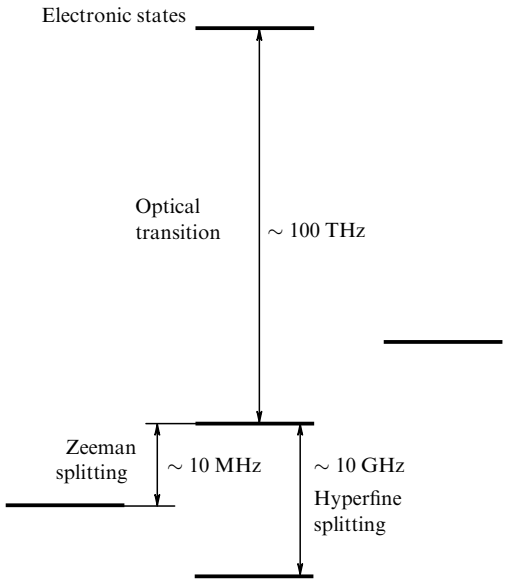

Figure 11. Characteristic level diagram of an ion indicating various transitions that can be used to encode and control qubits.

3.1.1 Multilevel system for encoding quantum information. The structure of levels in ions allows the use of many more than two levels, thereby encoding information in a d-level system. Such multilevel systems are usually called *qudits*. Qudits can be used to scale up quantum computers without significantly changing or complicating the experimental setup.

There are two main ways to use multilevel systems. The first is based on the fact that one qudit can be represented as $\log_2(d)$ qubits [69, 111]. For example, one ququart (a four-level qudit) can be represented as two qubits. Using one ion to encode several qubits at once allows the number of qubits to be increased to a hundred or several hundred with the existing technologies. In addition, qubits encoded in a single ion can be entangled using single-qudit operations, whose fidelity is usually significantly higher than that of two-particle entangling gates.

The second advantage of qudits is the possibility of using additional levels as auxiliary ones to reduce the number of gates required to perform quantum algorithms. These auxiliary levels are usually called ancilla. Thus, using qutrits (qudits with three levels) allows effectively reducing the number of operations required to perform the Toffoli gate, which is used in many quantum algorithms [112, 113].

The two approaches can be used simultaneously. For example, when using ququints (five-level qudits), the first four levels can be represented as two qubits, and the last auxiliary level can be used as an ancilla [114].

The main criteria for selecting levels for a qudit are their long coherence time and the ease of individual addressing and excitation of transitions between the qudit levels. It is important to note that different states of qudits can have different coherence times. For example, in [72] and [115], magnetic sublevels from the D-term are used to encode a qudit whose energies have different sensitivities to magnetic field fluctuations, which often determine the coherence time. Magnetic screens made of a μ-metal are often used to stabilize the magnetic field by reducing the effect of external magnetic fields [116, 117]. Active stabilization of the magnetic field is also possible using a pair of coils and a feedback loop, which allows precise control of the current through the coils [118]. The most effective way to reduce the influence of magnetic field fluctuations is to use dynamical decoupling methods [65, 119, 120]. In these methods, the qubit (or qudit) is encoded in protected superposition states that are weakly sensitive to the magnetic field.

There are several laboratories in the world developing a quantum computer on qudits. A group led by Blatt created a processor on 7-level qudits [121] in $^{40}Ca^+$ ions. Senko's group created a 13-level qudit in $^{137}Ba^+$ ions [115]; they claim that they can increase the number of qudit levels to 25. The first qudit quantum processor on $^{171}Yb^+$ ions was demonstrated in our laboratory [72]. A quantum computer with 8 ququarts (16 qubits) was also demonstrated [66], and a 50-qubit ion quantum computer, also based on the qudit architecture, was demonstrated as a result of the Roadmap implementation (see Section 5.1).

3.2 Initialization of quantum states

After the loading procedure, the ion register must be prepared in the initial state $|\psi_0\rangle$. An error associated with the quality of the preparation and readout procedures of the state of one ion, e_{SPAM} (state preparation and measurement error), leads to a decrease in the fidelity of the algorithms performed on the register, exponentially dependent on the number of qubits as $(1-e_{\mathrm{SPAM}})^{N_q}$, where N_q is the number of qubits, and leads to a systematic shift in the probability distribution of obtaining certain output states. Because this error is typically time stationary, the output data can be post-processed to correct the resulting distribution, but this leads to a sharp increase in the number of measurements that must be made. A requirement for implementing error correction algorithms is to perform a readout procedure during the execution of the quantum algorithm (mid-circuit measurement and reset), and therefore errors associated with the fidelity and speed of the state initialization procedure, as well as readout, contribute significantly to the error budget [97].

Typically, initialization of ion qubit states to the initial state $|\psi_0\rangle$ is performed using the optical pumping method [122]. Current experiments with ion qubits demonstrate the ability of this platform to implement the initialization procedure easily and efficiently: the initialization and readout fidelities achieved so far are better than those demonstrated on any other physical platform. Typical initialization errors for the ion platform are currently on the scale of 10^{-4} [24]. Recently, high-precision qubit manipulation based on the hyperfine state of the ^{133}Ba ion was demonstrated in [123], where the e_{SPAM} was measured to be 0.99971(3), and a method for achieving high-precision state preparation and measurement using the ^{137}Ba ion was presented in [124] to achieve an e_{SPAM} of $(9.0 \pm 1.3) \times 10^{-5}$.

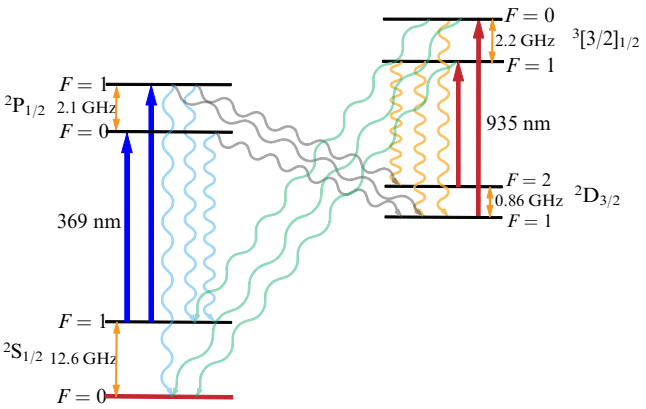

Figure 12. Scheme of optical pumping of ^{171}Yb ion to $^2S_{1/2}$ state ($F = 0, m_F = 0$) (marked in red). Solid lines show levels coupled by laser radiation, wavy lines show spontaneous decay processes.

Also, the electronic structure of a chosen ion and a chosen optical pumping method are important characteristics that affect the efficiency of the initialization procedure. For example, in our setup, the ^{171}Yb ion qubit can be easily and efficiently initialized by optical pumping to a single Zeeman sublevel ($F = 0$ and $m_F = 0$). The scheme of optical pumping of the ^{171}Yb ion is shown in Fig. 12. The ^{171}Yb ion has nuclear spin $I = 1/2$, which leads to a singlet ground state and allows simple and efficient initialization of the qubit state [122, 125].

3.3 Ion cooling

3.3.1 Doppler cooling. An important factor when working with an ion is the possibility of cooling it. Most often, the first stage is Doppler cooling, which requires the presence of a strong cyclic transition accessible to modern laser sources (such transitions exist, for example, in the ions Yb^+, Ca^+, Be^+, Ba^+, Sr^+, Cd^+, In^+, Mg^+, Hg^+, and Rb^+). However, for the Al^+, Na^+, and Th^+ ions, molecular ions, and some other particles, such transitions cannot be excited using existing lasers. In this case, sympathetic cooling can be used, which is discussed in the next section.

Due to the Doppler effect, the frequency of the electromagnetic field radiation experienced by a particle is different when moving toward the wave front and when moving in the same direction with the wave. It is then possible to tune the radiation frequency to the red range of the spectrum, such that the particle absorbs photons only when moving toward the beam, reducing its kinetic energy. When moving in the opposite direction, the effective tuning only increases and photons are not absorbed. If the re-radiation process is isotropic, then cooling occurs.

The equilibrium temperature of the ion depends on the radiation detuning Δ from the resonance of the atomic transition,

$$k_B T = \frac{\hbar\Gamma}{8}\left[(1+s)\,\frac{\Gamma}{\Delta} + \frac{4\Delta}{\Gamma}\right], \tag{18}$$

where s is a dimensionless parameter determined by the radiation intensity, wavelength, and natural cooling transition width Γ.

At the detuning value

$$\Delta_m = -\frac{\Gamma}{2}\sqrt{1+s}, \tag{19}$$

the minimum possible temperature is reached, given by the so-called Doppler limit

$$T_{\mathrm{m}} = \frac{\hbar\Gamma\sqrt{1+s}}{2k_{\mathrm{B}}}\,, \tag{20}$$

which, at characteristic widths of cooling transitions in ions of the order of several tens of MHz, is of the order of 1 mK. The first chain of cooled ions in Russia (see Fig. 2) was obtained at the Lebedev Physical Institute in 2016 [126].

For certain quantum operations on ions, cooling of the particle to the vibrational ground state is required. For light particles, such as the $^9Be^+$ ion, the Doppler limit temperature in terms of the average vibrational number can correspond to $\bar{n} \sim 0.5$ [33, 127]. However, for most particles, characteristic values are $\bar{n} = 10$–100, depending on the ratio of the cooling transition width to the secular frequency of the ion motion in the trap [128]. Accordingly, methods for achieving sub-Doppler temperatures need to be considered.

3.3.2 Resolved sideband cooling (RSC). When a particle is kept in a trap, its electron levels are split into many vibrational sublevels. If the width of the atomic transition turns out to be much smaller than the secular frequency of the ion motion in the trap, $\Gamma \ll \omega$, the so-called resolved sideband regime (RSR) is realized, meaning that transitions between individual vibrational components can be excited. Particle cooling is achieved by exciting the ion at the red sideband frequency and repumping it back to the initial electronic state, which, in average, occurs without changing of motional number. In this case, the particle loses one vibrational quantum during the cooling cycle. The resolved sideband regime can be realized by direct interaction with a narrow, most often dipole-forbidden, transition [129] optical RSR, or by using schemes that give a narrow effective line in comparison with the natural width of involved transitions, for example, Raman transitions [130, 131] (Raman RSR). Mathematically, the cooling process can be described as follows: after Doppler cooling, a thermal distribution over vibrational sublevels is established. The population of a specific sublevel can be found as

$$P_n = \frac{\bar{n}^n}{(\bar{n}+1)^{n+1}}\,, \tag{21}$$

where the dimensionless parameter $\bar{n}$ is the average vibrational number. When exposed to a laser pulse tuned to the first red sideband, the population of the level $|n\rangle$ transfers to $|n-1\rangle$ with the probability $R_{n\to n-1}$, and from the level $|n+1\rangle$ to $|n\rangle$ with the probability $R_{n+1\to n}$. Then, the new population can be found as $P_n \to P_n + P_{n+1}R_{n+1\to n} - P_nR_{n\to n-1}$, where

$$R_{n\to n-1} = \sin^2\left(\frac{\Omega_{n,n-1}t}{2}\right). \tag{22}$$

Here, t is the pulse duration, optimally equal to $\pi/\Omega_{n,n-1}$, and $\Omega_{n,n-1}$ is the Rabi frequency corresponding to the transition between these vibrational levels. The general formula for the dependence of the Rabi frequency for the transition between different vibrational states is given by the Debye–Waller coefficients [131]

$$\Omega_{n',n} = \Omega_0 \exp\left(-\frac{\eta^2}{2}\right)\sqrt{\frac{n_<!}{n_>!}}\,\eta^{|n'-n|}\,L_{n_<}^{|n'-n|}(\eta^2)\,. \tag{23}$$

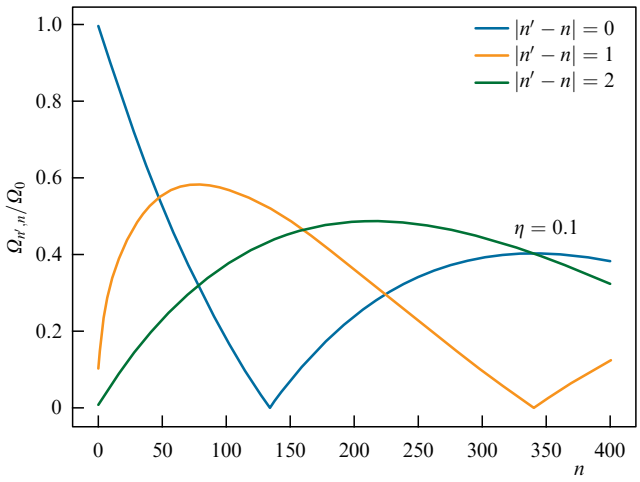

Figure 13. Dependence of relative Rabi frequencies for transition without a change in vibrational state (blue curve), first (orange), and second (green) red sidebands on the vibrational level number.

Here, Ω_0 is the Rabi frequency of the atomic transition without taking the contribution of vibrational states into account, $n_>$ ($n_<$) is the larger (smaller) of n' and n, and L_n^α are the generalized Laguerre polynomials

$$L_n^\alpha(X) = \sum_{m=0}^{N}(-1)^m\binom{n+\alpha}{n-m}\frac{X^m}{m!}\,. \tag{24}$$

The dependence of the Rabi frequency of the carrier transition, as well as of the first and second red sidebands, on the level number n is shown in Fig. 13.

It can be seen that, for certain values of n, the Rabi frequencies vanish. This means that the cooling pulse does not transfer the population to the lower levels, which would lead to population accumulation at $n \neq 0$ and a decrease in the efficiency and depth of cooling. The solution is to alternately use pulses with a detuning of one or two vibrational quanta. Theoretically, the achievable value of the average vibrational number is given by

$$\bar{n} \approx \left(\frac{\Gamma}{2\omega_{r,z}}\right)^2\left[\left(\frac{\tilde{\eta}}{\eta}\right)^2 + \frac{1}{4}\right]. \tag{25}$$

Here, $\tilde{\eta}$ is the Lamb–Dicke coefficient for the decay, which can differ from η if the ion returns to the initial state via auxiliary transitions. Finding the optimal pulse sequence is a complex multiparameter problem [131, 132]. Often, a sequence close to the optimal one can be determined experimentally, using the reasoning that a pulse tuned to the second red sideband does not excite the transition from the vibrational level $n = 1$, and therefore is less effective at the end of cooling.

By performing spectroscopy of the blue and red resolved sidebands after cooling, the average vibrational number can be determined from the ratio of the peak intensities,

$$\frac{P^{\mathrm{red}}}{P^{\mathrm{blue}}} = \frac{\bar{n}}{\bar{n}+1}\,, \tag{26}$$

and from the dephasing of Rabi oscillations [133]. For many ions, a value $\bar{n} < 0.05$ has been experimentally demonstrated [131, 134–136].

The disadvantage of this method is that only one vibrational mode is involved in the cooling process. Thus, cooling all the modes of a long ion chain takes a significant amount of time. There are ways to reduce this time by parallel cooling of several vibrational modes [137]. However, a more attractive approach is cooling by the electromagnetic-induced transparency method, where modes are cooled simultaneously within a fairly wide frequency range.

3.3.3 Cooling by electromagnetic-induced transparency method. The idea of cooling by the electromagnetically induced transparency (EIT) method is to create an absorption profile such that events where the particle loses vibrational energy are more probable than events where it is absorbed. Such a profile can be created in a three-level Λ scheme (Fig. 14). The achievable value of the average vibrational number can be determined by the rate equation method. It follows from (23) that the interaction with the nth sideband frequency is suppressed by the factor η^{2n}. To a first approximation, one can consider only carrier transitions as well as the first red and blue sideband transitions, ignoring others. The carrier transitions, accordingly, do not change the population of the vibrational level, and for others, the coefficients of the rate equations can be written as

$$R_{n+1}^{n} = W(\Delta_{\mathrm{g}})\,\eta^2(n+1) + W(\Delta_{\mathrm{g}} - \omega_{r,z})\,\eta^2(n+1)\,,$$
$$R_{n-1}^{n} = W(\Delta_{\mathrm{g}})\,\eta^2 n + W(\Delta_{\mathrm{g}} + \omega_{r,z})\,\eta^2 n\,, \tag{27}$$

where $W(\Delta_{\mathrm{g}}) = \Gamma\rho_{\mathrm{ee}}(\Delta_{\mathrm{g}})$ and Δ_{g} is the detuning of one of the cooling laser components from the resonance of the atomic transition (see Fig. 14). They correspond to an absorption–emission act with a return to the initial electronic state when the vibrational number changes by 1: $|\mathrm{g}, n\rangle \to |\mathrm{e}, n \pm (0, 1)\rangle \to |\mathrm{g}, n \pm 1\rangle$. For the population of the vibrational level, we can then write

$$\frac{\mathrm{d}}{\mathrm{d}t}\,P_n = R_n^{n+1}P_{n+1} + R_n^{n-1}P_{n-1} - (R_{n-1}^{n} + R_{n+1}^{n})P_n\,. \tag{28}$$

In this case, the change in the average vibrational number can be found as

$$\frac{\mathrm{d}}{\mathrm{d}t}\,\bar{n} = \sum_{n=1}^{\infty} n\,\frac{\mathrm{d}}{\mathrm{d}t}\,P_n\,. \tag{29}$$

At equilibrium, we obtain

$$\bar{n}_f = \frac{W(\Delta_{\mathrm{g}}) + W(\Delta_{\mathrm{g}} - \nu)}{W(\Delta_{\mathrm{g}} + \omega_{r,z}) - W(\Delta_{\mathrm{g}} - \omega_{r,z})}\,. \tag{30}$$

It is evident that, if the conditions $W(\Delta_{\mathrm{g}} - \omega_{r,z}) \gg W(\Delta_{\mathrm{g}})$ and $W(\Delta_{\mathrm{g}} - \omega_{r,z}) \gg W(\Delta_{\mathrm{g}} + \omega_{r,z})$ are satisfied, $\bar{n} \ll 1$.

With one of the beams taken to be a low-intensity probe beam, the optimal parameters can be determined from the condition

$$\omega_{r,z} = \frac{1}{2}\sqrt{\Delta_{\mathrm{r}}^2 + \Omega_{\mathrm{r}}^2}\,, \tag{31}$$

where Δ_{r} and Ω_{r} are the detuning and the Rabi frequency for the second laser component. The absorption profile can be described by the function

$$W(\Delta_{\mathrm{g}}) \approx \frac{(\Delta_{\mathrm{r}} - \Delta_{\mathrm{g}})^2\Omega_{\mathrm{g}}^2\,\Gamma}{\alpha\left[(\Delta_{\mathrm{r}} - \Delta_{\mathrm{g}})^2\Gamma^2 + 4\left(\Omega_{\mathrm{r}}^2/4 - (\Delta_{\mathrm{r}} - \Delta_{\mathrm{g}})\Delta_{\mathrm{g}}\right)^2\right]}\,, \tag{32}$$

where α is the relative probability of decay to the state $|\mathrm{g}\rangle$. Substituting (32) into (30) allows expressing the attainable value of the average motional number in terms of the detuning value and the transition width

$$\bar{n}_f = \left(\frac{\Gamma}{4\Delta_{\mathrm{r}}}\right)^2. \tag{33}$$

As mentioned above, the advantage of this method is the cooling of oscillatory modes in a wide frequency range. Keeping the optimal parameters for a certain value of $\omega_{r,z}$ (the mode that needs to be cooled to the lowest temperature), we can use (32) and (30) to determine the cooling depth for other values of secular frequencies (Fig. 15).

Considering that this method is implemented via strong transitions, one can expect cooling to the level of $\bar{n} < 1$ for all oscillatory modes in the range of several MHz.

EIT cooling has been successfully demonstrated for Ca^+ ions with cooling depth $\bar{n} \approx 0.01$ [138, 139], Mg^+ ions ($\bar{n} \approx 0.04$) [140], and Be^+ ions ($\bar{n} \approx 0.3$) [141]. For ions with a more complex level structure, there are modifications of this scheme, for example, double EIT cooling for the $^{171}Yb^+$ ion, first proposed by our group in [142] and experimentally demonstrated in [143] with individual modes cooled to $\bar{n} = 0.04$ and all modes in the 3-MHz range, to $\bar{n} < 0.54$.

3.3.4 Sympathetic cooling. Not all ions have a suitable level structure for the implementation of the above-mentioned

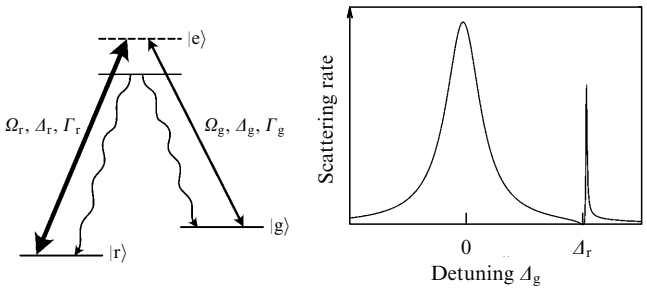

Figure 14. Optimized absorption profile for cooling using EIT method.

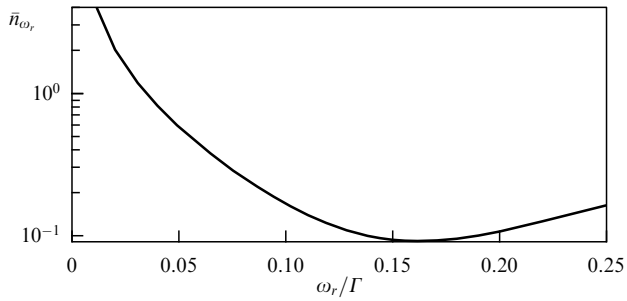

Figure 15. Dependence of cooling depth on ion oscillation frequency in a trap using EIT method for a certain fixed set of laser beam parameters.

Table 1. Implemented cooling methods for ions used in quantum computing.

Ion	Cooling method	Best result ($\langle n \rangle$)	References
Yb^+	Raman RSC, optical RSC, EIT	$\langle n \rangle \approx 0.04$	[143]
Ca^+	Raman RSC, EIT	$\langle n \rangle \approx 0.01$	[135]
Be^+	Raman RSC	$\langle n \rangle \approx 0.01$	[134]
Ba^+	Raman RSC, Optical RSC, EIT	$\langle n \rangle \approx 0.03$	[147]
Sr^+	Optical RSC	$\langle n \rangle \approx 0.13$	[136]
In^+	Sympathetic cooling	$\langle n \rangle \approx 0.30$	[148]
Mg^+	Raman RSC, sympathetic cooling	$\langle n \rangle \approx 0.03$	[146]
Al^+	Sympathetic cooling	$\langle n \rangle \approx 0.03$	[149]

cooling schemes. In addition, the particle state is destroyed during the cooling process, because the cooling cycle requires spontaneous decays. Due to the Coulomb interaction, ions continuously exchange kinetic energy with each other. In this case, a decrease in the energy for one ion leads to a decrease in the energy of the entire ion chain. Sympathetic cooling consists in applying one of the laser cooling methods to one or more ions to cool all ions in the chain. Sympathetic cooling can be used for a homogeneous ion crystal [144], but more often there are implementations with a chain of either two isotopes of the same substance or ions of two different substances [140, 145, 146]. In this case, there is no need for individual addressing of particles, because the resonance frequencies of the atomic transitions are different and the global excitation does not affect the electron states of sympathetically cooled ions. Sympathetic cooling is more efficient in the case of similar ion masses [145]. A noticeable difference in masses, although it increases the achievable temperature limit, has a number of advantages, for example, it allows detecting and compensating parasitic effects due to micromotion [146].

Table 1 summarizes information on experiments on cooling various ions, indicating the implemented cooling methods and the best temperatures achieved in terms of average vibrational numbers.

3.4 Readout of the ion states

Readout of qubit states is one of the most important procedures in the operation of a quantum computer, and the possibility of doing so is one of the DiVincenzo criteria. In addition to registering the particle state at the very end of the algorithm, a number of tasks also require mid-circuit readout of qubit subregisters during the execution of the algorithm (intermediate readout or mid-circuit measurement). Such tasks include, for example, quantum error correction. Thus, the fidelity of this procedure significantly affects the accuracy of the answer produced by executing the algorithm, the required number of task runs, and the possibility of error correction.

The ion qubit readout is based on the electron shelving [16]. To implement it, a strong cyclic transition is used, coupling one of the qubit states $|0\rangle$ or $|1\rangle$ to an auxiliary level $|\text{aux}\rangle$. Often, this is the same transition that is used for Doppler cooling. Without loss of generality, we assume that this transition is $|0\rangle \to |\text{aux}\rangle$. Under the influence of radiation in resonance with this transition, the qubit state is projected onto one of the states of the computational basis. If the qubit is projected into the $|0\rangle$ state, the ion starts scattering photons. Otherwise, the particle does not fluoresce. The radiation scattered by the ions is collected using high-aperture optics and registered using a highly sensitive detector, with a spatial resolution that allows individual particles to be detected. Such a detector can be either a highly sensitive camera (EMCCD, sCMOS, qCMOS) or an array of photomultiplier tubes (PMTs), avalanche photodiodes, or superconducting detectors. Analysis of the number of photons registered from each ion allows distinguishing between the $|0\rangle$ and $|1\rangle$ states of each particle.

The main characteristics of the readout procedure are its speed, the dead time between two successive registration procedures, and fidelity. The speed and the dead time become critical in the case of mid-circuit measurements, because qubits can decohere during the readout or dead time for the detector to recover. The typical readout duration for ions is about 40–5000 μs [7, 53, 150] and is limited by the quantum efficiency of the detectors, the efficiency of radiation collection, as well as parasitic illumination and dark noise. The current record readout speed is 46 μs with a resulting fidelity of 99.91% on the $^9Be^+$ ion [150]. Dead time is a limiting factor only due to the operation characteristics of chameras when these are used. The detection fidelity is affected by both technical factors such as stray light, dark noise of the detector, and fundamental limitations associated with parasitic population pumping between qubit states during readout [151], and spontaneous decay of one of the qubit states. Typical readout errors in commercially available devices are now of the order of 10^{-3} per ion [7, 152, 153], while the record readout fidelity is 99.991% [154] for the $^{40}Ca^+$ ion.

The detection speed and fidelity can be improved in various ways. For example, to improve fidelity, not only can information on the number of registered photons during the readout time be used, but so can their spatial and temporal distribution. Another promising direction is the integration of superconducting detectors directly into chip traps [155], which allows a significant increase in the efficiency of photon collection and improves the scalability of the system.

Qudits can be read out similarly to qubits; the implementation requires several stages. The first step is the same as reading out a qubit, and if fluorescence occurs, then the ion is considered to be registered in the state $|0\rangle$. If fluorescence does not occur, the population of the state $|1\rangle$ is transferred to the fluorescent state using the corresponding single-qudit operations, and the process is repeated. If fluorescence occurs, the ion is measured to be in state $|1\rangle$. Otherwise, a similar procedure is repeated for the level $|3\rangle$ and all subsequent ones except the last one, whose population can be determined from the normalization condition. An example of such a procedure is considered in more detail in Section 5.1.

4. Implementation of quantum gates with trapped ions

One of the requirements for a universal quantum computer is the ability to implement an arbitrary unitary operation on a quantum register in any quantum state (hence the term 'universal'). However, each such operation can be decomposed into a finite product of gates from the so-called *universal set* [156] of a much smaller size, and therefore the presence of these gates in the system ensures, in theory, that

any quantum algorithm can be executed. For example, such a set can contain all of the *one-qubit* gates together with one *two-qubit* CNOT gate, which is discussed in Section 4.3.1. Usually, the full set of one-qubit operations does not present any particular difficulty in implementation, because the parameters of these operations can be varied continuously over a wide range by the control electronics, and the quality of such gates does not depend much on these parameters. On the other hand, ensuring high fidelity of two-qubit gates is much more difficult and has been the subject of intensive research for a long time. The requirement of only one native two-qubit gate in the universal set significantly simplifies the task, because it allows one to focus on optimizing the fidelity of only the selected two-qubit operation when building a quantum computer.

4.1 Methods for implementing quantum operations

The type of quantum operation performed in a trapped-ion quantum computer depends on the internal electronic states in which the qubit is encoded. For a qubit realized on hyperfine components of the ground state, there are two manipulation methods: direct application of a microwave field with a frequency of about 1–10 GHz or stimulated Raman interaction with a laser field in the optical range (100–1000 THz). For an optical qubit, control is obviously performed by a laser field. We briefly describe each of the interactions and discuss their principal advantages and disadvantages.

Microwave gates. The idea of a microwave gate is the direct action on the ion by microwave radiation whose frequency coincides with or is close to the hyperfine splitting between the qubit states. The source of such radiation can be either a separate horn antenna far from the ions, or one of the electrodes of the trap itself, or special current-carrying wires located near the ions and providing near-field interaction [157]. Transitions between qubit levels in this setting are magnetic dipole, and therefore the most important characteristic of the wave is its magnetic field. Regardless of the type of source, the microwave field in the context of ion computing has an obvious drawback: the wavelength is much longer than the characteristic distance between ions, which makes individual addressing impossible. Errors from parasitic interactions with spectator neighboring ions is too large unless additional measures are taken. This problem can be circumvented by introducing a sufficiently large gradient of the static magnetic field, which separates the transition frequencies due to the Zeeman effect [158]. Another way to circumvent the addressing problem is to physically move the target ions into the region of high field amplitude using electronics, while spectator ions remain far from it. This method only works in the case of near-field sources.

The advantage of microwave gates is the lower (compared to laser gates) complexity in ensuring the stability of the frequency of the generator creating the field. High-precision commercial microwave generators are capable of attaining an error of several millihertz, providing a long qubit coherence time.

Raman gates. Gates on the Raman interaction operate due to the coupling of qubit levels $|0\rangle$ and $|1\rangle$ by two laser beams via some intermediate level $|e\rangle$ (Fig. 16). Conventionally, this intermediate level has a parity different from that of the qubit states, and hence electric dipole transitions between them are allowed. The frequency difference between the beams is close to the qubit splitting frequency, and the detuning Δ from the intermediate level is chosen to be large

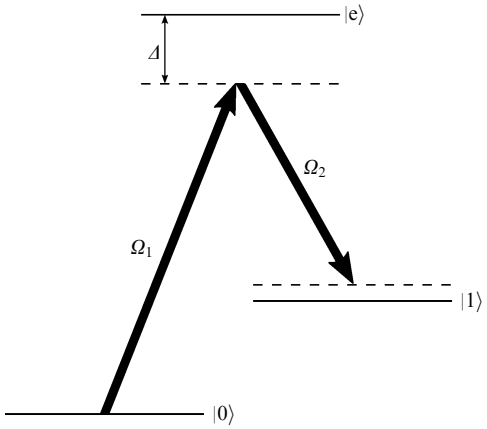

Figure 16. Schematic diagram of a Raman gate. Ω_1 and Ω_2 indicate laser beams that serve to couple qubit levels.

(1–100 THz), such that the photons of the laser field do not scatter due to resonance fluorescence, which would deteriorate the fidelity of operations. The interaction of a three-level system of a qubit and an additional level with such a pair of beams can be reduced in some approximations to the interaction of only the qubit system with a fictitious wave whose frequency is equal to the frequency difference among the waves in the beams, i.e., close to the qubit frequency, and the wave vector is equal to the difference between their wave vectors. If the beams are noncopropagating, the difference between the wave vectors can be quite large. As we show in Section 4.3.2, the magnitude of the wave vector characterizes the magnitude of the effect on an ion's motional degrees of freedom, which directly affects the speed and fidelity of two-qubit operations. The above-mentioned microwave gates do not work without a magnetic field gradient, because the coupling of the wave with ion motion is very weak due to the small wave vector, but such a problem does not occur in the case under consideration. Another advantage of Raman gates is the ability to individually address ions by focusing the radiation on the target ion (ions), which is much easier to achieve in the optical range. High stability of the beam frequency difference is guaranteed by the high stability of the generators driving the optical modulators, and the laser central frequency does not greatly affect the fidelity due to the high detuning from the levels. However, this system is not without its drawbacks. First, a large detuning requires a high laser power, and lack thereof would slow down the operations and increase their errors. Second, in most systems, the Raman beams are not copropagating, and hence any changes in the optical path difference of the beams would change the phase of the field at the ion's position, which can worsen the operation. In addition to active methods for correcting these errors [159], there are also methods for increasing the robustness of gates to Raman phase fluctuations [160], but this problem is present and complicates the setup of the system.

Optical gates. Similarly to microwave gates, optical gates involve interaction with the field whose frequency is close to the qubit frequency. In this case, the qubit is based on an optical transition, and hence a laser with the wavelength corresponding to the transition is sufficient to excite it. Here, as in the case of Raman gates, individual addressing of ions, as well as interaction with the vibrational degrees of freedom of ions, does not present any problems. The power required to

perform the operations is significantly less than for Raman gates. However, the absolute value of the phase noise of the laser is higher than that of the microwave generator, which reduces the qubit coherence time and also affects the fidelity of the operations. Systems with an optical linewidth of about 1 Hz (sufficient to control a qubit with a lifetime of ~ 1 s) exist and are widespread, but such stability is opposed by significant complexity and the increased cost of the setup [159].

4.2 Single-qubit and single-qudit gates

In this section, we consider single-qubit operations, i.e., operations performed on one individual ion. Most often, native single-qubit operations in ions are rotation operations. It is convenient to visualize the action of rotation operators as rotations on the Bloch sphere. The Bloch sphere is a representation of a single-qubit state (Fig. 17). An arbitrary qubit state can be written in the form

$$|\psi\rangle = \cos\left(\frac{\theta}{2}\right)|0\rangle + \exp(\mathrm{i}\phi)\sin\left(\frac{\theta}{2}\right)|1\rangle\,, \tag{34}$$

where θ is the polar angle and ϕ is the azimuthal angle.

4.2.1 Single-qubit operations. Rotations are usually divided into two types, which differ in their effect on states and their experimental implementation. Operations of the first type change the populations of states, while those of the second type only change the relative phase between them. The first type of operation is the rotation $R_\phi(\theta)$:

$$R_\phi(\theta) = \exp\left(-\mathrm{i}\,\frac{\theta}{2}\,\sigma_\phi\right) = \begin{pmatrix} \cos\left(\dfrac{\theta}{2}\right) & -\mathrm{i}\exp(-\mathrm{i}\phi)\sin\left(\dfrac{\theta}{2}\right) \\ -\mathrm{i}\exp(\mathrm{i}\phi)\sin\left(\dfrac{\theta}{2}\right) & \cos\left(\dfrac{\theta}{2}\right) \end{pmatrix}, \tag{35}$$

where $\sigma_\phi = \cos(\phi)\sigma_X + \sin(\phi)\sigma_Y$. The notation is taken from Nielsen and Chang's book [156]. Here, we use the classic notation for the Pauli matrices:

$$\sigma_X = \begin{pmatrix} 0 & 1 \\ 1 & 0 \end{pmatrix}, \quad \sigma_Y = \begin{pmatrix} 0 & -\mathrm{i} \\ \mathrm{i} & 0 \end{pmatrix}, \quad \sigma_Z = \begin{pmatrix} 1 & 0 \\ 0 & -1 \end{pmatrix}. \tag{36}$$

The rotation axis is in the equatorial plane, and its direction relative to the x-axis is determined by the angle ϕ. The angle θ determines how much the state rotates about the axis. For example, $R_{\phi=0}(\pi/2)$ specifies a rotation about the x-axis through $\pi/2$. For standard rotations about the x- and y-axes, the following notation is adopted: $R_x(\theta) = R_{\phi=0}(\theta)$ and $R_y(\theta) = R_{\phi=\pi/2}(\theta)$. The effect of $R_y(\pi/2)$ on the Bloch sphere is shown in Fig. 18.

There are different ways of performing the quantum operations that were discussed in Section 4: microwave, Raman, or optical gates. Single-qubit rotations $R_\phi(\theta)$ are realized using resonant Rabi oscillations, when the radiation frequency coincides with the qubit transition frequency (17).

The tilt angle of the rotation axis is determined by the initial radiation phase ϕ, and the rotation angle θ is given by the area under the $\Omega(t)$ graph. In the simplest case of a constant Rabi frequency, the rotation angle is $\theta = \Omega\tau$, where τ is the pulse duration. Therefore, adjusting the pulse duration, field phase, and laser power allows implementing an arbitrary rotation $R_\phi(\theta)$.

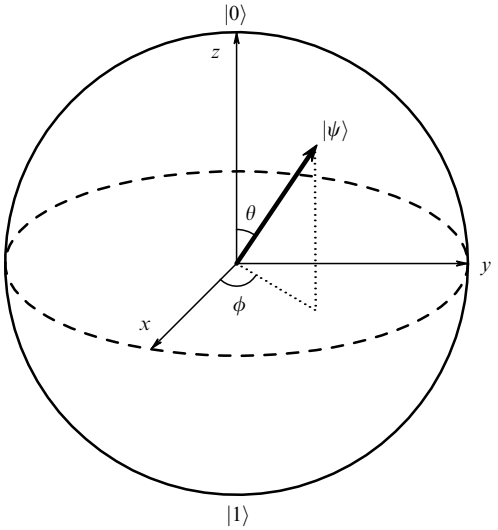

Figure 17. Visualization of arbitrary state $|\psi\rangle$ on Bloch sphere. North pole corresponds to state $|0\rangle$, and south pole, to state $|1\rangle$.

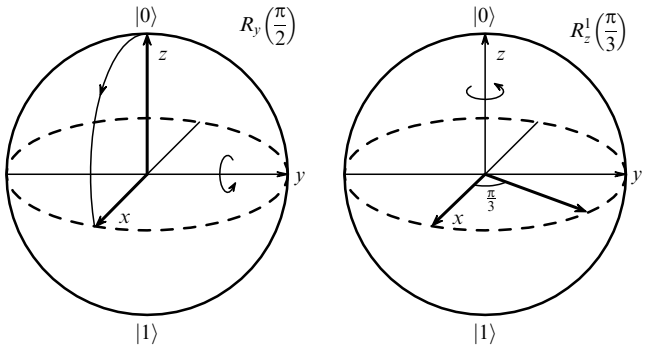

Figure 18. Example demonstrating action of single-qubit rotations. Bold arrow shows position of qubit on Bloch sphere before and after the operation. Light arrow shows axis about which rotation occurs. Type of rotation is written at top right.

The second type of single-qubit operation is $R_z(\theta)$:

$$R_z(\theta) = \exp\left(-\mathrm{i}\,\frac{\theta}{2}\,\sigma_Z\right) = \exp\left(-\mathrm{i}\,\frac{\theta}{2}\right)\begin{pmatrix} 1 & 0 \\ 0 & \exp(\mathrm{i}\theta) \end{pmatrix}. \tag{37}$$

The $R_z(\theta)$ rotation does not change the population of states, because the operator matrix is diagonal. The operator $R_z(\theta)$ can be viewed as the addition of a phase θ to the state $|1\rangle$. For example, the operator $R_z(\pi/3)$ rotates the state about the z-axis through $\pi/3$; its action on the Bloch sphere is shown in Fig. 18.

In the case of qudits, the operator $R_z^j(\theta)$ that adds a phase to the state $|j\rangle$ is used:

$$R_z^j(\theta) = \exp(\mathrm{i}\theta|j\rangle\langle j|)\,. \tag{38}$$

There are two ways to perform the rotation $R_z^j(\theta)$: virtual and real. Real rotation consists in applying a field that is tuned far from resonance and causes a Stark effect on the lower state.

This type of gate is called real because the rotation is realized by applying a field in a finite time.

A virtual method for effecting $R_z^j(\theta)$ is to rotate the coordinate system around the qubit state. This method was originally proposed for superconducting qubits [161] but is now used on all platforms. We consider the special case of the rotation $R_z^1(\theta)$ of the first state $|1\rangle$, which is equivalent to $R_z(\theta)$. Instead of rotating the qubit state through the angle θ, we can rotate the x- and y-axes through the angle $-\phi$. When executing the $R_\phi(\theta)$ gate, the direction of the ϕ-axis is controlled by the initial phase of the field. Therefore, rotating the x- and y-axes is equivalent to changing the phase of all fields involved in subsequent operations, both single-qubit and two-qubit, by $-\phi$. Changing the initial phase of the laser/microwave field can be done almost instantaneously, and hence virtual gates have zero duration and are much more efficient than real rotations about z-axis.

4.2.2 Single-qudit operations. The basic principles of executing quantum operations do not change when moving from qubits to qudits. Although a qudit cannot be visualized using a Bloch sphere, the notation for single-qudit operations was inherited from single-qubit operations.

In qudits, there is a rotation $R_\phi^{jk}(\theta)$,

$$R_\phi^{jk}(\theta) = \exp\left(-\mathrm{i}\,\frac{\theta}{2}\,\sigma_\phi^{jk}\right), \tag{39}$$

similar to the rotation $R_\phi(\theta)$, which is performed in the subspace of two levels $|j\rangle$ and $|k\rangle$. The implementation of this operation consists of a resonant excitation of the transition between two levels, everything else being similar to the qubit case. The operator $R_z^j(\theta)$ is independent of the qudit dimension, because it is carried out at one level. The implementation is similar to the qubit case.

To create a universal quantum qudit computer, it is necessary to be able to execute an arbitrary rotation $R_\phi^{jk}(\theta)$ between any levels $|j\rangle$ and $|k\rangle$. However, in an experimental setup, most often not all qudit states are directly connected. In what follows, by the qudit topology we mean a graph whose vertices are the qudit states. If it is possible to excite a transition between two levels, then these two vertices are connected by an edge. The topology is directly related to how the qudit is encoded (see Section 3.1 for details on various encoding methods).

For example, we consider the qudit topology in [115], where the qudit consists of 13 levels. In that setup, the state $|0\rangle$ is chosen in the ground term $^2\mathrm{S}_{1/2}$, and the excited states are chosen among the hyperfine structure of the $^2\mathrm{D}_{5/2}$ level. The excited states are not directly coupled to each other by a microwave field. In [115], all gates are optical, i.e., they are executed between the ground state $|0\rangle$ and any other state $|j\rangle$ using a laser at a wavelength of 1762 nm. The topology where one level is coupled to all the others is called the star topology. Such a topology of qudit levels is used in our work with ququarts [66, 72]. Blatt's group [121] used a double star topology, where two levels are connected to all others, and work on the two-qudit entangling operation [162] used a star topology. The star topology is often the simplest to implement, because it requires only one laser, which can be tuned in a large frequency range, so as to couple to all excited qudit levels from the Zeeman structure. The fully connected topology, despite its advantages in terms of the efficiency of algorithm execution, is usually not encountered in practice due to the technical complexity of implementation.

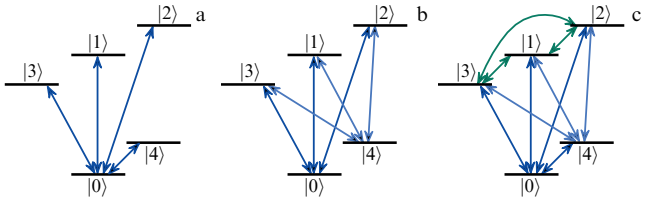

Figure 19. Qudit topologies (using a ququint as an example, $d = 5$). (a) Star topology [66, 115, 162], (b) double star topology [121], (c) fully connected topology.

4.2.3 Characterization of single-qubit operations. The term fidelity is used to characterize the quality of a quantum operation. The fidelity F of an operation is understood as a measure of how close the action of a real operation on a state is to the expected one. The fidelity is always between 0 and 1. If the operation was performed without errors, the fidelity is 1. The closer the fidelity is to 1, the more accurate the operation is and the less susceptible the quantum computer is to errors.

There are many ways to determine the fidelity of operations, including single-qubit ones, such as quantum tomography [163, 164], randomized benchmarking [165], or cross-entropy benchmarking [166]. Tomography involves initializing the quantum register to certain initial states, performing the operation, and then measuring in different bases. A series of measurements allows reconstructing the process channel. However, the disadvantages of tomography are that the result is affected by the auxiliary operations used in this procedure and the preparation and readout errors (SPAM), and also the exponential growth of the number of measurements with the number of qubits involved. Nevertheless, a number of approaches have been proposed that allow at least a partial solution to the tomography problems, such as gate set tomography [167]. Randomized and cross-entropy benchmarking, in turn, are based on running random chains of a certain type with different lengths on a quantum computer. From the dependence of the average accuracy of reconstructing the expected probability distributions of output states on the chain length, one can draw a conclusion about the fidelity of the operations. These methods scale significantly better to large systems and allow simultaneously taking SPAM errors into account, but provide less information about the process compared to tomography.

In addition to fidelity, important characteristics of any gate are its duration and parasitic effect on other qubits in the register. The depth of chains that can be run on a particular processor is limited by the coherence time of the system. Reducing the time of one operation allows performing a greater number of operations in one quantum chain. The characteristic duration of a single-qubit operation on ions is of the order of several μs or tens of μs. There are also ultrafast gates that were executed in 25 ps [168] with a fidelity of 99%.

The durations and fidelities of single-qudit operations achieved to date are shown in Fig. 20. The record-breaking fidelity of a single-qubit operation was achieved by Lucas's group [169] on a microwave qubit in a $^{43}Ca^+$ ion using a microwave antenna. In the work of the same group in 2023, microwave single-qubit operations on two ions with addressing without using a laser field were demonstrated [110]. In that paper, composite gates were used (further details about them are given in Section 4.2.4). The stars in the graph show the results of single-qudit rotations achieved on an ion computer developed in Russia within the Roadmap framework.

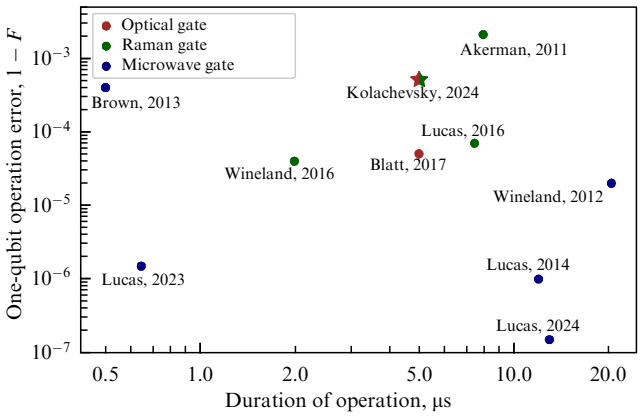

Figure 20. Accuracy and duration of single-qubit $R_x(\pi/2)$ operations on ions demonstrated to date. (Results from [24, 110, 168–176].) Color of symbols indicates type of gate, and heads of laboratories authoring the papers written are indicated next to the symbols. Asterisk indicates result of our laboratory.

4.2.4 Composite single-qubit pulses. The fidelity of quantum operations can be increased not only by improving the quality of the quantum gates themselves but also by specially constructing quantum chains that are significantly less sensitive to certain errors in the operations. In this section, we consider composite single-qubit operations that are composed of several gates and are less sensitive to certain types of noise.

Composite pulses were once proposed in nuclear magnetic resonance (NMR) protocols to suppress systematic errors but then found application in quantum information. The simplest example of a composite gate is the spin echo sequence [177], which consists of using a π-pulse to suppress phase noise. The spin echo method was actively used in NMR and is now used to suppress errors in two-qubit operations. For example, spin echo is effectively used in the LS gate [28, 178], which is discussed in more detail in Section 4.3.

Another example is composite gates that suppress amplitude errors. Amplitude errors are those in the rotation angle θ of the single-qubit rotation $R_\phi(\theta)$ from formula (35). They arise due to fluctuations in the amplitude of the field used to excite the transition, or due to an incorrectly calibrated pulse duration. The best-known schemes of composite single-qubit operations are the so-called BBn [179], SKn [180], PDn [181], and SCROFULOUS [182] sequences, which are used to suppress nth-order amplitude errors. First-order schemes are typically used, because, with an increase in the order of the scheme, along with the efficiency of suppressing amplitude errors, the total duration of the gate also increases. Therefore, when using higher-order schemes, the gain due to amplitude error suppression often starts being offset by the system decoherence during the operation. As an example, we discuss the SK1 scheme. It consists of performing a sequence of operations $R_{\phi+\phi_{SK}}(2\pi)R_{\phi-\phi_{SK}}(2\pi)R_\phi(\theta)$, where $\phi_{SK}(\theta)$ is calculated based on the desired rotation angle θ.

Another important feature of using composite gates is that some of these schemes, in addition to amplitude errors, allow suppressing crosstalk — the parasitic effect of the gate on other qubits in the register. When performing optical gates, the laser beam has a finite waist size, and hence the field partially affects other ions, which causes crosstalk. Crosstalk is also present for one reason or another when using microwave qubits. The SK1 scheme suppresses the influence of the gate on the ion at which the field amplitude is close to zero, which significantly reduces crosstalk.

There are also CORPSE sequences for suppressing the error of the transition detuning from resonance [179, 182] and generalized sequences that suppress both sources of error [183]. In all the above sequences, errors are assumed to be constant in time, i.e., the same for all gates of the same type. To suppress time-dependent errors, dynamically corrected gates (DCGs) are used [184–186].

Composite pulses have been demonstrated on ions experimentally and showed better fidelities than single pulses do. For example, in Lucas's 2023 paper, composite microwave pulses are used to suppress crosstalk [110]. The PD6 and BB1 sequences were used to improve the fidelity of the Raman gate [187], with the composite pulse error being one third that of the single pulse error. Dynamically corrected pulses were demonstrated experimentally, confirming the improvement in results when using the filter function [188].

4.3 Two-qubit gates

For a two-qubit gate to be implemented on two different ions, some interaction between them is required. This fact is obvious if we represent it in the language of quantum mechanics as follows. A two-qubit gate belonging to a complete set must be *entangling*, i.e., not representable as a tensor product of one-qubit operators. This means that the Hamiltonian leading to such an evolution operator must affect the degrees of freedom of both ions, i.e., be an interaction Hamiltonian.

In most modern ion systems, common motional modes of the ion chain in the trap are used as the interaction mechanism. The main reason for this choice is the ability to ensure full connectivity of qubits, regardless of the distance between them in the chain. Indeed, each motional mode is not a localized oscillation of certain ions, but a coordinated motion of all ion simultaneously, and hence the excitation of one or more of them changes the state of both ions considered for the operation. In this regard, common motional modes can be thought of as a quantum bus through which the interaction is transmitted from one ion to another. Below, we describe the best-known types of two-qubit gates on motional modes and the main achievements in their implementation, and also discuss the pros and cons of each approach.

4.3.1 Cirac–Zoller gate. The first implementation of a two-qubit operation on ions was the gate proposed in 1995 by Cirac and Zoller [15]. This gate was of great importance for the field of ion quantum computing, because it was the missing key piece for the direct physical implementation of an ion quantum computer in terms of the DiVincenzo criteria [189] and gave rise to a vigorous development of this field.

The gate works as follows. The quantum state of the entire ion chain is specified by all internal electron states of the ions, as well as the vibrational states of each common vibrational mode. The system of levels relevant for the gate on the selected ions A and B can be equivalently represented as a set of electron states, each of which is superimposed with a 'ladder' of vibrational levels of the oscillator (Fig. 21). The basis state of the system of two ions

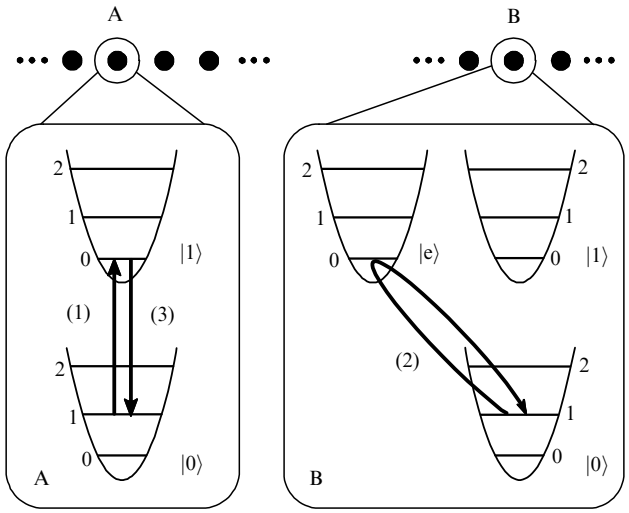

Figure 21. Schematic diagram of Cirac–Zoller gate. Arrows indicate laser pulses.

can be written as $|x_A x_B, n\rangle$, where x_A and x_B are the electronic qubit states of the ions, and n is the occupation number of the vibrational mode (here, one mode is considered). Before the gate starts, the mode is cooled to the ground vibrational state $n = 0$, then a three-stage sequence of actions is performed:

1. A laser pulse with a frequency lower than that of the qubit transition by exactly one mode frequency is sent to ion A (the so-called *red sideband*). As can be seen from Fig. 21, such a pulse couples the states $|1_A x_B, 0\rangle - |0_A x_B, 1\rangle$; all other initial states remain unchanged due to the absence of resonant interaction. The duration and power of the pulse are such that, if successful, the entire population is transferred from one level to another, i.e., a π-pulse is realized.

2. A 2π-pulse is performed on the B ion on the red sideband between $|0_B\rangle$ and $|e_B\rangle$, which is an auxiliary level with the allowed transition to $|0_B\rangle$. At this stage, only the state $|x_A 0_B, 1\rangle$ is affected, and applying a 2π-pulse does not change the population of the state; only the sign of the wave function changes.

3. Step 1 is repeated, returning the vibrational state of the chain to the initial one, and hence only the internal states of the ions change after the gate is implemented.

The above steps can be represented in the form of the following truth table (taking the phase $\pi/2$ due to each π-pulse into account):

$$\begin{array}{cccc} & \xrightarrow{(1)} & \xrightarrow{(2)} & \xrightarrow{(3)} \\ |0_A 0_B, 0\rangle & |0_A 0_B, 0\rangle & |0_A 0_B, 0\rangle & |0_A 0_B, 0\rangle \\ |0_A 1_B, 0\rangle & |0_A 1_B, 0\rangle & |0_A 1_B, 0\rangle & |0_A 1_B, 0\rangle \\ |1_A 0_B, 0\rangle & \mathrm{i}|0_A 0_B, 1\rangle & -\mathrm{i}|0_A 0_B, 1\rangle & |1_A 0_B, 0\rangle \\ |1_A 1_B, 0\rangle & \mathrm{i}|0_A 1_B, 1\rangle & \mathrm{i}|0_A 1_B, 1\rangle & -|1_A 1_B, 0\rangle \end{array}.$$

The matrix of this operator is

$$U_{CZ} = \begin{pmatrix} 1 & 0 & 0 & 0 \\ 0 & 1 & 0 & 0 \\ 0 & 0 & 1 & 0 \\ 0 & 0 & 0 & -1 \end{pmatrix}, \quad (40)$$

which corresponds to the matrix of the control–phase (CZ) gate. The transition to the CNOT gate is easy to make using the one-qubit Hadamard gate H [156]:

$$U_{CNOT} = (1 \otimes H) U_{CZ} (1 \otimes H) = \begin{pmatrix} 1 & 0 & 0 & 0 \\ 0 & 1 & 0 & 0 \\ 0 & 0 & 0 & 1 \\ 0 & 0 & 1 & 0 \end{pmatrix}. \quad (41)$$

The fidelity of a two-qubit quantum operation can be estimated as the fidelity of the preparation of some entangled state. This approach is much easier to implement in practice than the tomography or randomized methods described above and is often used in ion quantum computers, especially due to the relatively low speed of these devices and the resulting complexity of performing a large number of measurements required for characterization. In the simplest case of a pure state, the fidelity of the state preparation can be defined as

$$F = \left|\langle \psi_0 | \psi \rangle\right|^2, \quad (42)$$

where $|\psi\rangle$ is the actual final state and $|\psi_0\rangle$ is the ideal final state of the quantum register for a given initial state. The physical interpretation of expression (42) is clear from the probabilistic meaning of the wave function: fidelity is the probability of obtaining the target state from a given initial state. For the mixed state with a density matrix ρ, the fidelity is

$$F = \langle \psi_0 | \rho | \psi_0 \rangle. \quad (43)$$

In practice, fidelity is measured in two steps. The first consists in measuring the populations of the states of the two-qubit subsystem after implementing the gate without modifications, thereby obtaining the diagonal elements of ρ. The second step is similar to the first but involves additional analysis pulses, which allows determining the off-diagonal elements of ρ [39].

The first experimental confirmation of the possibility of implementing the Cirac–Zoller gate was demonstrated in 2003 by Blatt's group [32]. They used an optical qubit in the $^{40}Ca^+$ ion at a wavelength of 729 nm, and the gate itself was realized on a chain of two ions. They used a higher-frequency axial mode where the ions oscillate out of phase (the so-called breathing mode). The gate fidelity in this experiment was $F = 0.71(3)$.

Despite its importance in the history of ion quantum computing, the Cirac–Zoller gate is not used in practice in any modern system. The main reason is the stringent requirement of cooling the chain to the ground vibrational state. Efficient cooling methods giving average occupation numbers $\overline{n} < 0.1$ had been considered previously [138, 143, 190–192], but such methods are quite complex to implement and do not scale well to longer ion chains due to weaker coupling of the radiation to the sidebands and due to high heating rates [193]. In addition, for long chains, the axial frequency must be very small (see Eqn (11)), which makes the gate slow. An attempt to use a gate on radial modes suffers from the problem of having a large number of closely spaced modes (see Fig. 5), which increases the probability of nonresonant parasitic interactions with nontarget modes.

4.3.2 Gates on a spin-dependent force. One of the reasons why the Cirac–Zoller gate requires cooling the chain to the ground vibrational state is that, during its operation, the entire population is transferred to a specific vibrational level resonantly. To ensure stability against ion temperature,

another type of gate is needed, which uses vibrational states not directly, but *virtually*, i.e., as intermediate ones. This class of ion gate is called gates on *spin-dependent force* and is described below.

The basic idea of spin-dependent force gates is to apply *bichromatic* laser radiation (radiation with two frequency components) to the ion chain, which drives forced oscillations of a certain mode with a phase dependent on the internal state of the ion (hence the term spin-dependent force). Under certain conditions, if several ions are illuminated, their internal states are entangled at the end of such an interaction, and the vibrational states return to the initial ones. This is the main advantage of such gates. The two most common configurations are described below.

Mølmer–Sørensen (MS) gate. A gate proposed in 1999 by Mølmer and Sørensen [27] uses bichromatic components detuned from the main electronic transition by a frequency $\pm\mu$ that is close to the vibrational frequency of the mode. Accordingly, the average frequency of such components is equal to the transition frequency, $2\omega_0 = \omega_\mathrm{r} + \omega_\mathrm{b}$, where ω_0 is the qubit frequency, ω_r is the lower of the laser frequencies, and ω_b is the higher one. When two ions in a chain are illuminated, this field provides a Raman-type transition between states $|00, n\rangle \leftrightarrow |11, n\rangle$ via intermediate states with a changed vibrational number, as shown in Fig. 22. Under certain relations between the gate time, the detuning, and the laser power, entanglement of the electronic states of the ions can be ensured by terminating such a Raman process 'in the middle,' without vibrational degrees of freedom being excited.

The effective Hamiltonian of the interaction of two ions with a laser field in this formulation has the form [194]

$$\hat{H}_\mathrm{MS} = -\sum_{j=1,2} \hbar\eta_j \Omega_j \cos\left(\mu t + \phi_\mathrm{M}^{(j)}\right)\left(\hat{a}\exp\left(-\mathrm{i}\omega t\right) + \hat{a}^\dagger \exp\left(\mathrm{i}\omega t\right)\right)\hat{\sigma}_\phi^{(j)}, \tag{44}$$

where Ω_j is the Rabi frequency of the laser field acting on a given ion, $\hat{a}$ and $\hat{a}^\dagger$ are the ladder operators of the vibrational mode, ω is its frequency, and η_j is the Lamb–Dicke coefficient of the jth ion. The remaining quantities are expressed in terms of the phases of the bichromatic components $\phi_\mathrm{r}^{(j)}$ and $\phi_\mathrm{b}^{(j)}$ as

$$\phi_\mathrm{M}^{(j)} = \frac{\phi_\mathrm{r}^{(j)} - \phi_\mathrm{b}^{(j)}}{2}, \quad \phi_\mathrm{S}^{(j)} = \frac{\phi_\mathrm{r}^{(j)} + \phi_\mathrm{b}^{(j)}}{2},$$
$$\hat{\sigma}_\phi^{(j)} = \hat{\sigma}_x^{(j)} \sin\phi_\mathrm{S}^{(j)} + \hat{\sigma}_y^{(j)} \cos\phi_\mathrm{S}^{(j)}. \tag{45}$$

In the leading order, the evolution under such a Hamiltonian is effected by the operator [178]

$$\hat{U}_\mathrm{MS} = \hat{D}(\alpha\hat{S})\exp\left(2\mathrm{i}\chi\hat{\sigma}_\phi^{(1)}\hat{\sigma}_\phi^{(2)}\right). \tag{46}$$

Here, $\hat{D}$ is the displacement operator in the phase space of the vibrational mode. The eigenvalues of $\hat{S}$ have different signs, depending on the electronic state. Accordingly, for two eigenstates with opposite eigenvalues, the displacements are the same in magnitude, equal to $|\alpha|$, but opposite in sign (Fig. 23), which is a consequence of the spin dependence of the force. The phase χ is called the entanglement phase and serves as the main parameter of the gate, because it determines the degree of quantum entanglement of the two states. It can be shown [39] that this phase is proportional to the area swept by the radius vector of the displacement trajectory on the phase plane (Fig. 23). A necessary condition for the correct operation of the gate is the complete closure of the phase trajectory, so as to have $\alpha = 0$ and $\hat{D} = 1$. In this case, for example, the initial state $|00\rangle$ with $\chi = \pi/8$ and with a certain choice of qubit phases gives rise to the maximally entangled Bell state

$$|\psi_0\rangle = \frac{|00\rangle + \mathrm{i}|11\rangle}{\sqrt{2}}. \tag{47}$$

The full form of the MS gate matrix with this χ is

$$U_\mathrm{MS} = \frac{1}{\sqrt{2}}\begin{pmatrix} 1 & 0 & 0 & \mathrm{i} \\ 0 & 1 & \mathrm{i} & 0 \\ 0 & \mathrm{i} & 1 & 0 \\ \mathrm{i} & 0 & 0 & 1 \end{pmatrix}. \tag{48}$$

This matrix can be reduced to CNOT by one-qubit operations, which allows using this gate in the complete set.

Light-shift gate. Another gate, called the light-shift (LS) gate, operates similarly to the MS gate described above. In its simplest formulation, it is based on coupling one qubit state to some intermediate upper level by bichromatic radiation (Fig. 24). The difference between the bichromatic components is close to the mode frequency, and hence the ion is subject to the Stark effect, oscillating with the frequency of the mode (hence, 'light shift' in the name). The Stark effect results in the force exerted by the field oscillating with the same frequency, but only when the ion is in a state coupled to the intermediate one, while, in another qubit state, the radiation does not lead to the Stark effect. This is possible in two cases: either the detuning from the intermediate level is much smaller than the qubit transition frequency, and the

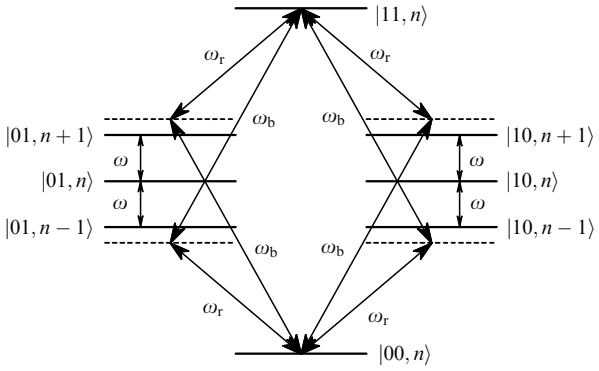

Figure 22. Schematic diagram of MS gate levels. Bichromatic field creates four Raman paths between states $|00, n\rangle \leftrightarrow |11, n\rangle$. Levels $|01, n\rangle \leftrightarrow |10, n\rangle$ are related similarly.

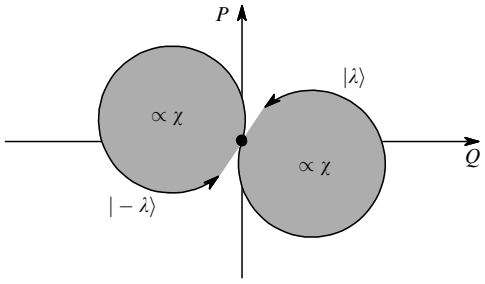

Figure 23. Evolution of vibrational eigenstates of operator $\hat{S}$ with opposite eigenvalues $|\pm\lambda\rangle$ on phase plane. Circular trajectory corresponds to constant radiation power.

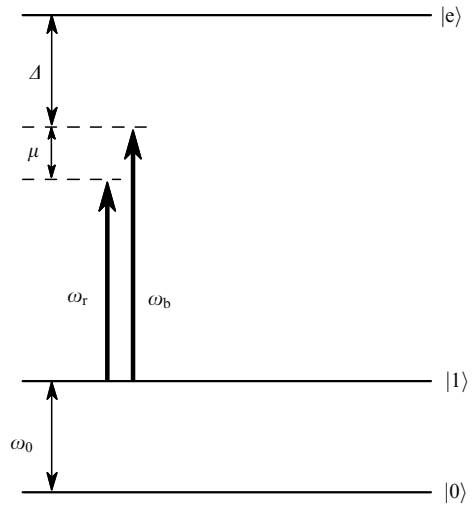

Figure 24. LS gate setup. Bichromatic frequency difference is $\mu \approx \omega$, where ω is mode frequency. Detuning Δ is large compared to $|1\rangle \leftrightarrow |e\rangle$ transition width and compared to laser Rabi frequency for this transition.

second state is then far from resonance, or the qubit and the radiation polarization are chosen such that one of the transitions is forbidden by selection rules.

Thus, the configuration described above leads to a spin-dependent force that entangles states in a manner similar to the MS gate. The difference is in the form of the evolution operator

$$\hat{U}_{\mathrm{LS}} = \hat{D}(\alpha\hat{S}) \exp\left(2\mathrm{i}\chi\hat{\sigma}_z^{(1)}\hat{\sigma}_z^{(2)}\right). \tag{49}$$

Instead of the product $\sigma_\phi \otimes \sigma_\phi$, the exponent contains the product $\sigma_z \otimes \sigma_z$. When choosing $\chi = \pi/8$, the gate matrix becomes

$$U_{\mathrm{LS}} = \begin{pmatrix} 1 & 0 & 0 & 0 \\ 0 & -\mathrm{i} & 0 & 0 \\ 0 & 0 & -\mathrm{i} & 0 \\ 0 & 0 & 0 & 1 \end{pmatrix}. \tag{50}$$

This matrix can also be reduced to CNOT by one-qubit rotations. The LS gate can be considered equivalent to the MS gate, but in a rotated basis.

Comparison of MS and LS gates. Although the LS and MS gates are mathematically equivalent, the practical implementation of each of them can be completely different for physical reasons or depending on the details of the experiment. For example, the LS gate in the above-described setting is much easier to implement on an hyperfine qubit. The frequency of such a qubit is low enough to use a single laser source and change its spectrum using modulators by implementing one-qubit and two-qubit operations. In an optical qubit, the qubit transition wavelength is very different from the LS gate radiation wavelength. For the correct operation of a quantum computer, phase matching at the specified wavelengths is necessary. Such matching is possible in principle, but it requires at least an optical comb [195], which significantly complicates the setup. The MS gate, in turn, is explicitly implemented with the same laser sources that are used in one-qubit operations, with only minor modifications to their spectrum. In addition, the difference among the Stark shifts of the qubit levels leads to an additional shift in the one-qubit phases during the gate execution. Such a phase affects all subsequent quantum operations, which means that the quality of the algorithm is sensitive to laser power fluctuations. In the MS gate, with equal beam powers, this effect is absent.

Figure 25. Optimal beam geometry for LS gate on hyperfine qubit. Interference of bichromatic components creates a quasi-standing wave that moves along axis of selected mode and creates a periodic spin-dependent force acting on ions.

It is worth noting that, for an optical qubit, there are variants of two-qubit operations that are similar to the LS gate and allow overcoming the problem of using several laser sources [178], but they have slightly worse parameters in comparison to the MS gate. These parameters include the required radiation power and the ratio of the strength of the useful coupling ensuring entanglement to the parasitic one, which reduces the fidelity of the operation.

We also note that, due to the equality of the polarizabilities of the states of a hyperfine qubit with a zero projection of the magnetic moment (clock transition states), it is impossible to implement an LS gate on such a qubit. To implement an LS gate at hyperfine levels, one has to select magneto-sensitive states [196, 197], which affects the fidelity of operations due to magnetic field fluctuations. The MS gate does not have such a limitation.

In addition to the above-mentioned disadvantages of the LS gate compared with the MS gate, there are a number of advantages. First, for a hyperfine qubit, the optimal geometry of bichromatic components corresponds to an antiparallel scheme (Fig. 25) in both cases (LS and MS). Consequently, the effective Lamb–Dicke parameter is twice that of a single beam, which allows using less optical power for the same gate time or reducing the time at a fixed power compared to a single modulated beam. In such geometry, the LS gate requires laser modulation at the motional mode frequency, i.e., of the order of several MHz, which does not cause difficulties due to the wide availability of optoelectronics at these frequencies. If the MS gate is implemented in the same configuration of antiparallel beams in order to increase the effective Lamb–Dicke parameter, then modulation at the level of several GHz is required to ensure the Raman interaction.

Second, the MS gate, in contrast to the LS gate, in addition to interactions on the red and blue sidebands, involves interaction at the carrier frequency, and hence the transition between qubit levels is excited nonresonantly without changing the vibrational number. It is evident from Fig. 22 that, if the Rabi frequency of one of the bichromatic beams is comparable to the mode frequency ω, then there is a substantial probability of transitions $|x0, n\rangle \leftrightarrow |x1, n\rangle$ and $|0x, n\rangle \leftrightarrow |1x, n\rangle$, where $x \in \{0, 1\}$. These transitions degrade the fidelity of the operation, because they do not involve the motional modes through which entanglement between ions is transmitted. In the LS gate, due to the large difference between ω and the qubit frequency ω_0, such an effect is absent.

Third, the LS gate, by design, has no dependence of the gate parameters on the optical phases of the lasers [160]. This fact plays an important role when executing long sequences of gates, which can lead to slow drifts experienced by the phases. These drifts do not affect the LS gate if they are small on the scale of its duration, and the influence of phase fluctuations from gate to gate or from sequence to sequence is suppressed

in such a setup. There are ways to suppress the influence of fluctuations for MS gates as well [160, 178], but such schemes require either a change in the geometry of the beams, which is not always possible, or additional compensating pulses, which lengthens the sequence.

Experimental implementations. The two main qualities of two-qubit operations, which are given primary attention, are the gate time and fidelity. For ions, it is also important to mention the chain length on which the gates are executed, because, for larger arrays, the gates are worse and slower on average. The spin-dependent force gate was first implemented earlier than the Cirac–Zoller gate, namely, in 2000 by Monroe's group [198]. The gate was implemented on beryllium ions $^{9}Be^{+}$ with a qubit realized on the hyperfine sublevels of the ground state with a splitting of 1.25 GHz. The frequency of the selected mode (breathing mode) was 8.8 MHz. In the original paper, not only a two-qubit but also a four-qubit MS gate was implemented, which works similarly to a two-qubit gate, with the difference being that all four ions in the chain are illuminated. The respective fidelities obtained in the experiment were 0.83 and 0.57 for two and four ions. A variant of the LS gate, also called the *geometric phase gate*, was first implemented by Wineland's group in 2003, also on beryllium ions [39]. The qubit hyperfine sublevels were chosen in such a way that the average Stark shift of both levels could be made the same by choosing a specific laser field polarization. At short times, the force exerted by the beams depends on the ion's internal state. The chain consisted of two ions, and the mode frequency was 6.1 MHz. The gate time was 39 μs. The authors managed to achieve a fidelity of 0.97 in this experiment, which was significant progress in the field at that time.

Presently, there is a fairly large set of implementations of the described gates with high fidelity and a fairly short duration. The highest fidelity values were obviously obtained in laboratory conditions on very small systems not intended for carrying out quantum algorithms. Nonetheless, there are large-scale ion quantum processors whose fidelity is not much worse. For example, the latest commercially available version of the recently created H2 computer [6] by Quantinuum has 56 qubits with full connectivity and a minimum fidelity of 0.997 for all-pairs two-qubit operations [153]. Another company, IonQ, has been providing access to the latest model of the Forte computer [152] since 2022, with 36 fully connected qubits and a two-qubit gate fidelity of 0.996 [199]. These and other selected demonstrations of high-fidelity gates with their characteristics are listed in Table 2.

Table 2. Selected demonstrations of two-qubit gates on a spin-dependent force.

Gate type	Fidelity	Duration, μs	Ion	References
MS	0.996	—	$^{40}Ca^{+}$	[200]
MS	0.993	50	$^{40}Ca^{+}$	[37]
MS	0.997	30	$^{9}Be^{+}$	[172]
MS	0.999	25	$^{171}Yb^{+}$	[201]
MS	0.998	—	$^{171}Yb^{+}$	[6]
MS	0.996	680	$^{171}Yb^{+}$	[152]
LS	0.999	100	$^{43}Ca^{+}$	[171]
LS	0.98	2.13	$^{43}Ca^{+}$	[202]
LS	0.997	90	$^{171}Yb^{+}$	[28]
LS	0.996	35	$^{40}Ca^{+}$	[162]
LS	0.998	49.2	$^{43}Ca^{+} + {}^{88}Sr^{+}$	[203]
LS	0.9994	35.2	$^{40}Ca^{+}$	[204]

5. 50-qubit ytterbium ion quantum computer

5.1 Quantum computer on $^{171}Yb^{+}$ ions

One important result of the implementation of the 2020–2024 Roadmap for Quantum Computing in Russia was the creation of an ion quantum computer on ytterbium ions, which is capable of working with quantum registers of up to 50 qubits. A set of original solutions were developed when creating this computer. For example, the use of an optical quadrupole transition at a wavelength of 435.5 nm for encoding information [67] (Fig. 26), the qudit architecture [69, 72], an original scheme for continuous dynamical decoupling of magnetically sensitive qudit states [65], and a method for stabilizing secular frequencies of an ion trap were designed and implemented. It is also important to note that, in the course of this work, we acquired competence in building ion traps with low heating rates and high secular frequencies, creating highly stable laser systems for controlling quantum states of particles, automating calibration processes and quantum computing, and executing quantum operations on ion arrays of several dozen particles.

The described computer is based on a linear bulk Paul ion trap. The trap was made of copper and coated with a gold. The developed design ensures high accuracy of the electrode geometry, high thermal and electrical conductivity of electrodes, and good optical access to the captured particles (Fig. 27). The distance from the electrode surface to the trap axis is $r_0 = 250$ μm. The radial confinement electrodes are in the form of four blades located symmetrically around the axis, while axial confinement is ensured by two endcap electrodes. A hole is provided in the center of the endcap electrodes to ensure optical access to ions along the trap axis. The trap is mounted on a vacuum flange equipped with a set of electrical inputs and a specially designed intravacuum objective with a numerical aperture of 0.2 for individual optical addressing of particles. The flange also has a copper tube connected to the trap to provide cooling and thermal stabilization, which is an important feature distinguishing this system.

For the $^{171}Yb^{+}$ ion, the maximum radial and axial secular frequencies are 4.4 MHz and 370 kHz, respectively. In the

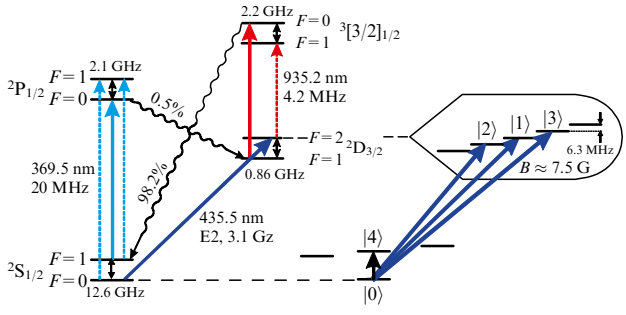

Figure 26. Level diagram of $^{171}Yb^{+}$ ion used to encode information in the created quantum computer. Quantum information is encoded in Zeeman sublevels $|0\rangle$, $|1\rangle$, $|2\rangle$, and $|3\rangle$ of $^{2}S_{1/2}(F=0)$ and $^{2}D_{3/2}(F=2)$ states. $|4\rangle$ state is used as an ancilla in some algorithms. Light blue line corresponds to laser radiation used for Doppler cooling, initialization, and readout of ion states. Red line shows pumping laser radiation, and dark blue ones are laser fields used to perform quantum operations. Wavy lines correspond to spontaneous decays, and dotted lines are radiation obtained by phase modulation of corresponding laser sources.

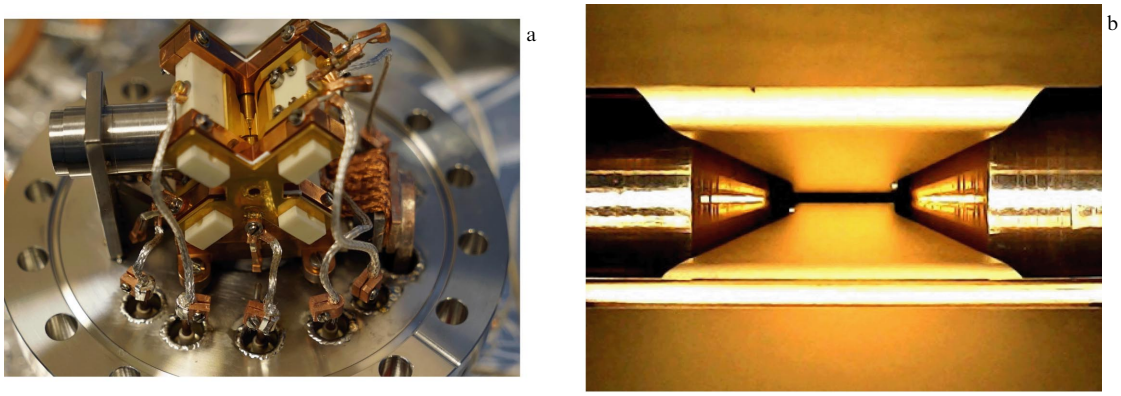

Figure 27. Photographs of ion trap used in constructed 50-qubit computer. (a) Photograph of flange with trap assembled on it, as well as intra-vacuum objective for individual addressing. (b) Photograph of trap electrodes.

experiments described below, secular frequencies $\omega_{\{x;y;z\}} = 2\pi \times \{3.7; 3.6; 0.13\}$ MHz were used when working with 10 ions and $\omega_{\{x;y;z\}} = 2\pi \times \{2.7; 2.6; 0.13\}$ MHz when working with 25 ions. The heating rate of a single ion in the radial direction at a secular frequency of 3.7 MHz was $\dot{n} = 23 \pm 3$ phonons per second [66]. The stability of the radial secular frequencies is maintained at a level of about 100 Hz for times of the order of several hours using active stabilization of the confining potential amplitude by following a scheme similar to the one described in [205].

The trap is installed in a vacuum chamber, the pressure in which is maintained at a level of less than 10^{-10} mbar using an ion-getter pump. Inside the chamber, a magnetic field with induction $B = 7.5$ G is maintained, created by a system of permanent magnets, which is necessary to remove the degeneracy in Zeeman sublevels and avoid the effect of coherent population trapping during Doppler cooling and readout the state of qudits [206]. Fluctuations and drift of the magnetic field are partially compensated by an active stabilization loop consisting of a three-axis sensor and three pairs of coils in the Helmholtz configuration. The spectrum of residual field fluctuations, whose average amplitude is about 1 mG, is dominated by harmonics at multiples of 50 Hz, created by power supply interference, which is to some extent leveled by synchronizing the beginning of each experimental cycle with the phase of the AC-line.

Ions are captured in the trap by the method of two-color selective photoionization of the ytterbium atomic beam from the oven at wavelengths of 399 nm and 369.5 nm. Doppler cooling of ions at the beginning of each cycle is performed using a 369.5-nm laser phase-modulated at 14.7 GHz to avoid population trapping in the $^2S_{1/2}(F = 0)$ state, and a 935-nm pumping source, which is also phase-modulated at 3.7 GHz to pump population from the $^2D_{3/2}(F = 2)$ metastable state. The same laser sources (but in a different modulation mode) are used to initialize the $|0\rangle = {}^2S_{1/2}(F = 0, m_F = 0)$ state before executing the algorithms and readout [68, 160]. A ququart is encoded in the states $|0\rangle$, $|1\rangle = {}^2D_{3/2}(F = 2, m_F = 0)$, $|2\rangle = {}^2D_{3/2}(F = 2, \ m_F = -1)$, and $|3\rangle = {}^2D_{3/2}(F = 2, m_F = 1)$ (see Fig. 26). Another ancilla level $|4\rangle = {}^2S_{1/2}(F=1, m_F=0)$ is also available, used in some quantum algorithms. The coherence time of the $|0\rangle \to |1\rangle$ transition is 31 ms, and that of the $|0\rangle \to |2\rangle$ and $|0\rangle \to |3\rangle$ transitions is 1 ms without active noise suppression schemes and 9 ms when using continuous dynamical decoupling schemes [65].

The 369.5-nm photons scattered during the readout and cooling procedure are collected using a high-aperture (0.48 numerical aperture) objective. The image of the ion chain is projected either onto a high-sensitivity camera matrix or onto an array of multimode fibers arranged nonequidistantly according to the positions of the particles in the crystal (Fig. 28). The other ends of these fibers are connected to individual channels of a PMT, which allows the fluorescence of each individual ion to be registered. The use of a fiber array together with a PMT ensures a low level of dark counts and virtually no dead time between successive readout cycles (at the level of 8–16 ns), which is important for readout of the qudit states and also makes it possible to record the arrival time of each individual photon. However, this approach is poorly scalable, because changing the number of ions in the register requires replacing the fiber array. The array currently in use is designed to work with 10 ions. Camera readout is a much more scalable technique and allows working with larger ion arrays (a camera is used for readout when working in the 50-qubit mode), although it has a number of disadvantages, the main one being a dead time between frames of about 1 ms, as well as higher dark noise, which leads to lower readout fidelity, especially in the qudit mode.

Quantum operations on the ion register are performed using a highly stable laser system at a wavelength of 435.5 nm (Fig. 29). It is based on a diode laser with an external cavity at a wavelength of 871 nm, whose frequency is stabilized with respect to a highly stable optical cavity made of ultra-low expansion glass by the Pound–Drever–Hall method similar to the one described in [207]. The relative instability of the laser frequency was less than 3×10^{-15} at averaging times from 1 to 100 s when measured relative to another reference laser at a wavelength of 1140 nm using a femtosecond optical comb. Within the Roadmap framework, an important technology for filtering fast phase noise of a laser source was implemented based on injection locking of an auxiliary laser diode to radiation passed through a highly stable cavity [208]. This allows significantly suppress the high-frequency laser noise, which strongly affects the fidelity of both single-qudit and two-qudit operations. Figure 30 shows a graph characterizing noise suppression due to filtering.

The computer supports two types of single-qudit operations. The first is $R_\phi^{0k}(\theta), k = 1, 2, 3$, implemented by applying a resonant laser pulse between the levels $|0\rangle$ and $|k\rangle$ to some ion using an individual addressing beam. The parameters ϕ and θ are respectively defined by the optical phase and pulse

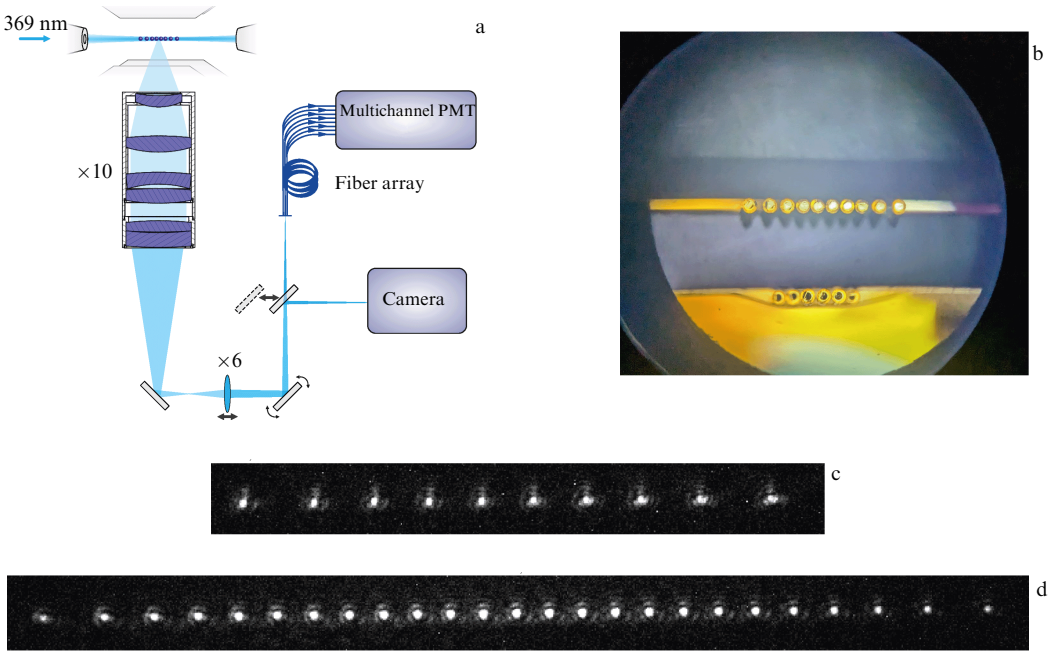

Figure 28. Ion fluorescence registering system. (a) General diagram of readout system. Switching between highly sensitive camera and PMT is performed using motorized mirror. (b) Photograph of 10-ion readout fiber array. (c, d) Images of 10- and 25-ion registers obtained with a camera.

duration. The composite form of such a gate is also supported with the SK1 scheme, which allows suppressing the cross-talks on neighboring ions and the effect of pulse power calibration errors, but it extends the operation time, which negatively affects the ratio of the gate time to the coherence time (with the typical duration of a conventional $R_\phi^{0k}(\theta)$ gate given by 12 μs, its composite form takes about 55 μs, including the time required to change the beam phase). The second supported type of gate is a virtual operation $R_z^j(\theta)$ on some ion.

Figure 31 shows the results of randomized benchmarking of the single-qudit operation $R_\phi^{01}(\theta)$ on an arrays of 10 and 25 ions. The fidelities of single-qudit operations on different ions agree with each other to within the error. The fidelity of single-qudit operations on a register of 10 ions, $F_{\mathrm{SQ}_{10}} = 0.99946(6)$, exceeds the result for 25 ions, $F_{\mathrm{SQ}_{25}} = 0.9985(2)$, due to the lower contribution of residual particle motion to the error.

In addition to such operations performed with individual addressing, it is also possible to perform global operations on all particles simultaneously, $R_\phi^{0k}(\theta)$, $k = 1, 2, 3, 4$, where the $R_\phi^{04}(\theta)$ operation is executed using a microwave pulse, which is useful for implementing some algorithms, examples of which are discussed below.

The processor also supports a two-qudit MS operation on the transition $|0\rangle \to |1\rangle$. This gate is implemented by applying a bichromatic laser field to a selected pair of ions using individual addressing beams. To account for the influence of all motional modes, as well as to suppress errors associated with secular frequency fluctuations, amplitude modulation of the bichromatic pulse is used in the implementation of the gate. The full connectivity of qubits in the processor is realized.

Figure 32 shows the fidelity table of two-qubit operations on a 10-ion register for all possible pairs. The operation fidelity was estimated by measuring the accuracy of the Bell state preparation by applying the $XX(\pi/4)$ operation to a selected pair of ions initialized in the $|00\rangle$ state. The preparation accuracy was calculated similarly to [209] with correction for the preparation and readout error. Table 3 shows the results of characterizing the fidelity of two-qubit operations for several pairs of ions in the 25-qudit (50-qubit) mode. The population dynamics of the qudit states during the two-qudit operation and the parity oscillations between pairs with numbers 5 to 21 are shown in Fig. 33. Generally, the fidelities obtained in the 25-qudit mode are lower than in the case of 10 ions, which is due to a more complex vibrational spectrum and its lower stability caused by the electrode charging under the action of laser beams and the corresponding change in the axial vibration frequencies.

To improve the fidelity of quantum operations in each experimental cycle, immediately before the implementation of the algorithm, the radial vibrational modes are cooled to the average vibrational number $\bar{n} < 0.1$. For this, the cooling method is implemented on the $|0\rangle \to |1\rangle$ transition at the resolved sideband frequencies.

After all operations are performed, the state of each qudit is read out. This procedure is schematically shown in Fig. 34. The fidelities of readout with a PMT and a camera are shown in Fig. 35.

The created computer was integrated with a cloud platform that allows quantum circuits defined with a graphical editor or using the QASM2.0 language to be automatically transpiled to native operations and run on a quantum device, with the obtained results displayed.

5.2 Implementation of basic quantum algorithms

The created computer (both the 50-qubit version and its previous generations) was used to implement a number of quantum algorithms. First of all, a number of benchmarking tasks were launched aimed at assessing the performance of the device. These included, in particular, the Bernstein–Vazirani algorithms [66] and the Grover algorithm with both phase [66] and Boolean oracles [29].

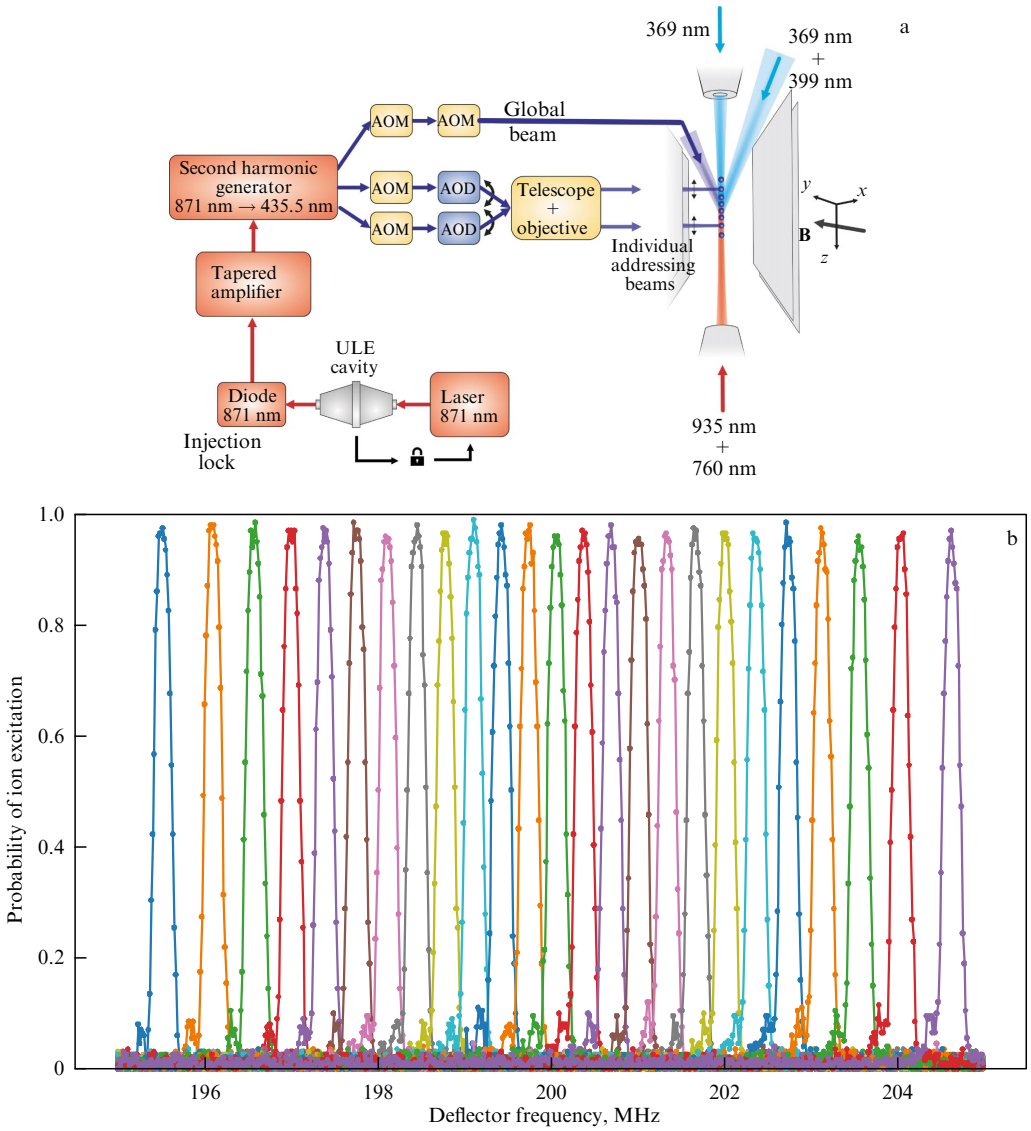

Figure 29. (a) Diagram of ion addressing system and injection of laser beams into a Paul trap. (b) Dependence of excitation probability of each of 25 ions in the trap (shown in different colors) when scanning AOD frequency, which corresponds to scanning individual addressing beam along ion chain. Plot shows 25 well-resolved peaks, demonstrating possibility of individual addressing of each ion in the trap.

In our work [66] in 2023 on an 8-qudit (16-qubit) generation of the computer, we demonstrated a two-qubit Grover algorithm with qubits encoded in different ions with a phase oracle, attaining an average implementation fidelity of 83%. This algorithm provides a polynomial gain compared to its classical analogues in the problems of searching through unordered databases and finding the inverse function. The quantum circuit corresponding to this algorithm contained two two-qudit operations. In 2024, already using a 10-qudit (20-qubit) processor, a three-qubit Grover algorithm with a Boolean oracle was implemented [29]. The qubits were again encoded in different ions, which allows studying the noisiest mode of the computer. Despite the increased complexity of the algorithm, the increased number of entanglement operations (three $XX(\pi/2)$ operations and one $XX(\pi/4)$ operation) and the larger dimension of the Hilbert space used (the original method for implementing the multiqubit Toffoli gate was used, reducing the number of entanglement operations by using an additional ancilla level), the overall fidelity remained at the level of 83%, which was achieved by increasing the fidelity of operations in parallel with the increase in the number of qudits.

Another common algorithm used to characterize quantum computers is the Bernstein–Vazirani algorithm. It allows reconstructing the key in a single evaluation of the oracle that returns the scalar product of the input register with a certain secret key. In [66], the results of running a two-qubit version of this algorithm were presented with the qubits encoded both in different ions and in one ion in the 8-qudit (16-qubit) generation of the computer. The fidelity of the task execution when encoding information in a single particle using qudits (97%) was expectedly higher than when using traditional two-level encoding (95%). This is due to the absence of the need for two-particle entanglement operations.

Figures 36 and 37 show the results of running several circuits via the cloud platform, corresponding to the three-qubit Bernstein–Vazirani algorithm and the two-qubit Grover algorithm. These experiments were carried out during an experimental demonstration of the 25-qudit (50-qubit) pro-

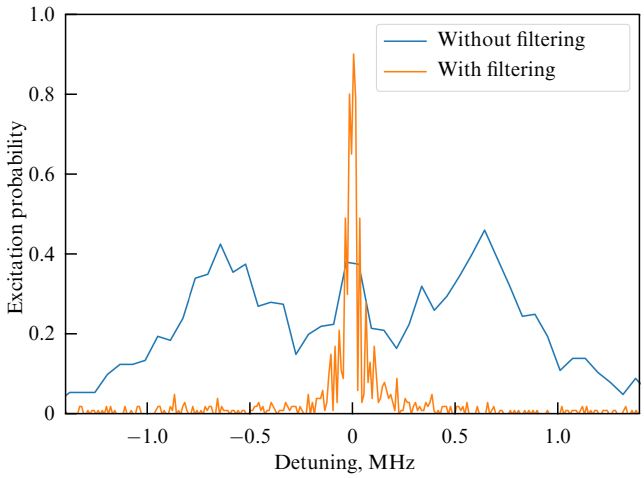

Figure 30. Probability of excitation of $|0\rangle \to |1\rangle$ transition in ion vs detuning from transition by a 400-μs laser pulse with π-pulse duration of 11 μs for a laser without and with high-frequency noise filtering. This experiment allows estimating magnitude of laser phase noise, because all excitation at detunings greater than 50 kHz with these parameters is entirely determined by interaction of phase noise with carrier. It is evident that filtering allows suppressing noise to a level below detection threshold.

cessor. In both cases, each qubit was encoded in a separate ion, with a full register of 25 particles in the trap. The most significant contribution to the error in this case was made by the readout error and secular spectrum fluctuations arising from photoinduced parasitic electric fields.

The computer was also used to solve quantum chemistry problems. In particular, using the iterative quantum assisted eigensolver algorithm [210–213], the ground state energies of the H_2 and LiH molecules [68] were calculated to within chemical accuracy. In the first case, two of the 8 ions were used in the trap, and in the second case, five of the 8 ions were used. The calculation results are given in [66].

The use of the computer also made it possible to conduct a number of experiments in the field of quantum machine learning. Studies were conducted to compare various ways of mapping classical input data into the Hilbert space of the quantum computer for these problems. In particular, the problem of classifying images of handwritten digits 0 and 1 using the support vector machine method was considered.

Table 3. Fidelities of two-qudit operations in 25-qudit (50-qubit) regime for several pairs.

Ion numbers	Fidelity without SPAM correction	Fidelity with SPAM correction
5–21	92 ± 2%	97 ± 3%
7–19	88 ± 3%	93 ± 4%
9–22	84 ± 3%	90 ± 4%

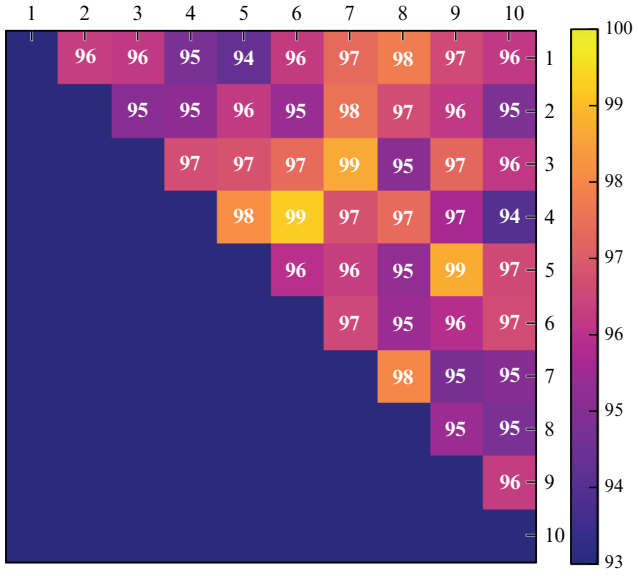

Figure 32. Fidelity table of two-qudit $XX(\pi/4)$ operations between all possible pairs of ions in 10-qudit (20-qubit) regime. Assessment was made by evaluating accuracy of Bell state preparation. Error of each value is ±2%. Average fidelity of two-qubit operation on the array was 96.3 ± 0.3%.

The kernel matrix was calculated using the quantum computer [68]. The efficiencies of various schemes for encoding classical information were compared. In all cases, a classification accuracy of 100% was achieved.

Experimental studies were conducted in the field of optimization and sampling problems. The sampling accuracy of the output histograms of quantum circuits typical for solving problems using the quantum approximate

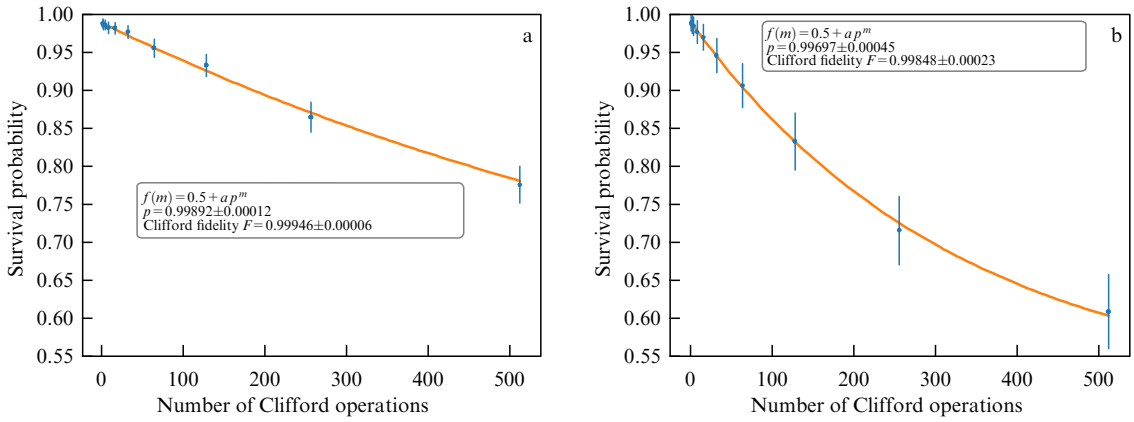

Figure 31. Probability of registering ions in $|0\rangle$ state vs number of random Clifford operations in a circuit within framework of randomized benchmarking of single-qudit operations $R_\phi^{01}(\theta)$ on array of (a) 10 ions ($F_{SQ_{10}} = 0.99946(6)$) and (b) 25 ions ($F_{SQ_{25}} = 0.9985(2)$). Fidelities of operations for all ions in register are the same (to within the error).

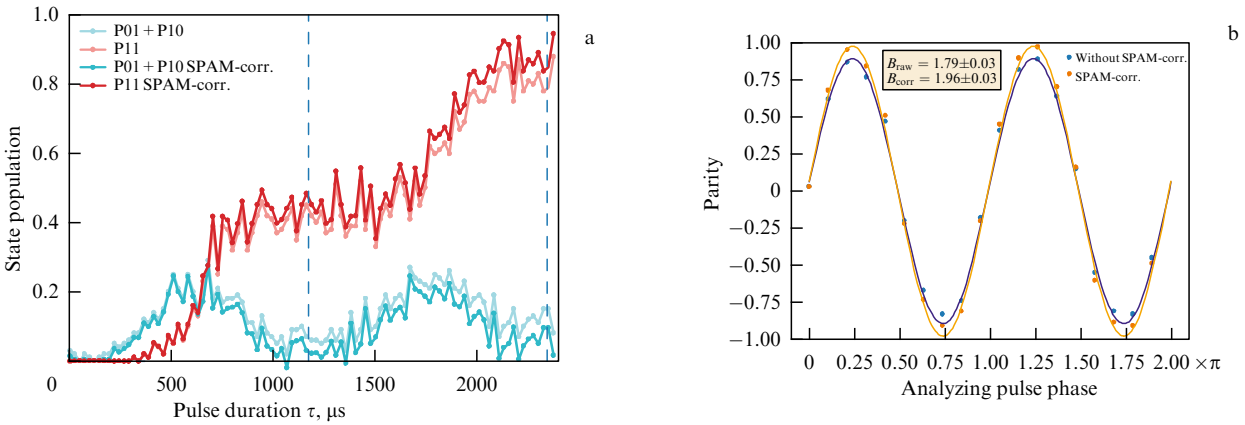

Figure 33. (a) Population of $|11\rangle$ state and total population of $|01\rangle$ and $|10\rangle$ states of qudit pair 5–21 in register of 25 ququarts vs duration of bichromatic pulse used for entanglement. $XX(\pi/4)$ gate corresponds to pulse duration of 1172 μs (vertical dashed line). (b) Parity oscillations (probabilities of finding ions in states $|11\rangle$ and $|00\rangle$ minus populations of states $|01\rangle$ and $|10\rangle$) on a pair of ions 5–21, obtained by applying $XX(\pi/4)$ gate to a pair of ququarts and then analyzing $R_{\phi}^{01}(\pi/2)$ gate, whose phase is scanned, to both particles.

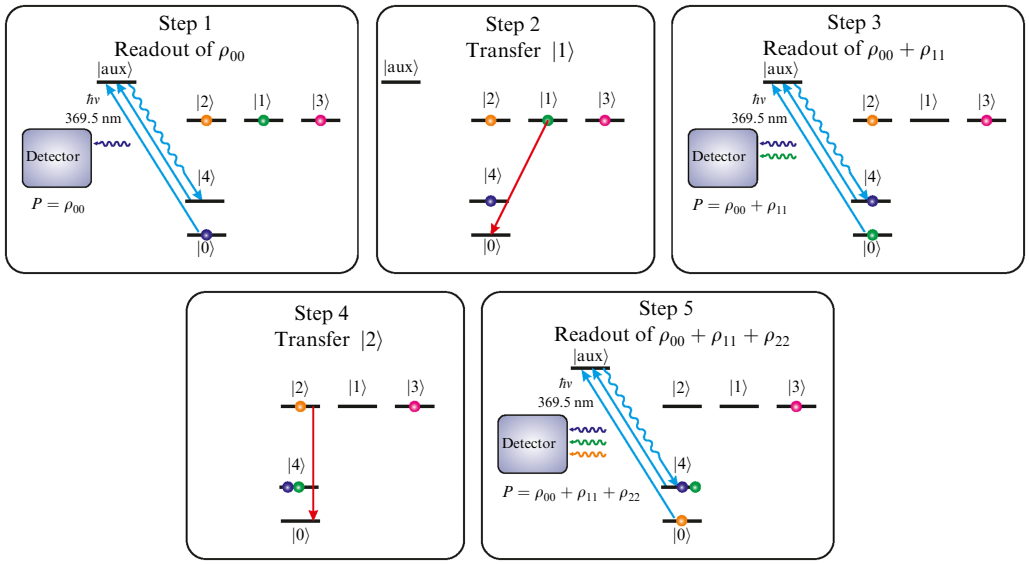

Figure 34. Schematic illustrating procedure for ququart state readout. Procedure consists of several cycles, in the first of which population of the state $|0\rangle$ is read out, and then total population of $|0\rangle$ and $|1\rangle$ states, and subsequently of $|0\rangle$, $|1\rangle$, and $|2\rangle$ states is read, and the population of last state is calculated from normalization condition. We set $|\text{aux}\rangle = |^2\text{P}_{1/2}\rangle$ $(F = 0)\rangle$ and $|4\rangle = |^2\text{S}_{1/2}(F = 1, m_F = 0)\rangle$.

Figure 35. Results of measuring SPAM error in the case of ququart coding using (a) a PMT and (b) a camera. Time of one photon registration cycle is $\tau = 1$ ms. Additional error when using camera is due to dead time of 1 ms and spontaneous decays of $^2D_{3/2}$ level during this time.

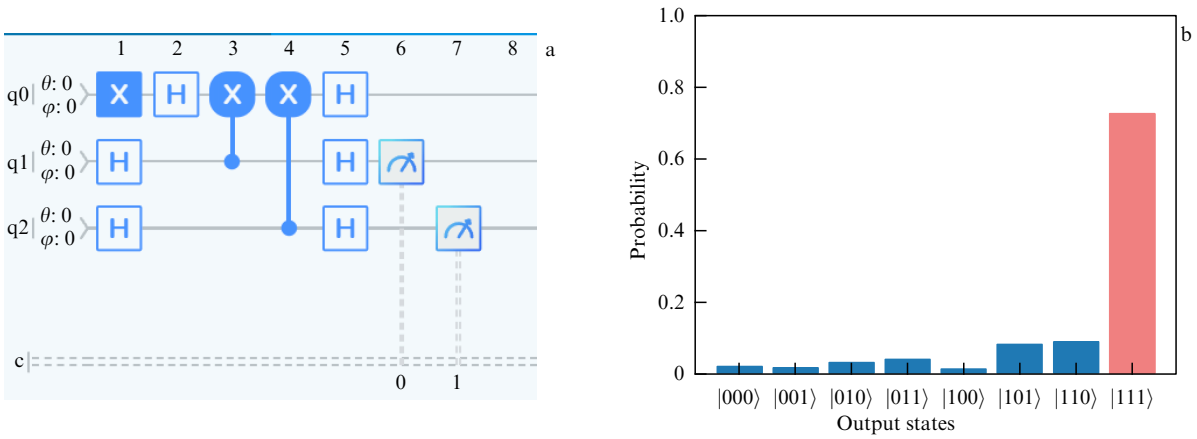

Figure 36. (a) Screenshot of graphical editor of cloud platform used to prepare circuit corresponding to Bernstein–Vazirani algorithm with key 11. (b) Results of executing quantum circuit. Histogram is based on 1024 repetitions of the circuit. Expected output state is shown in red.

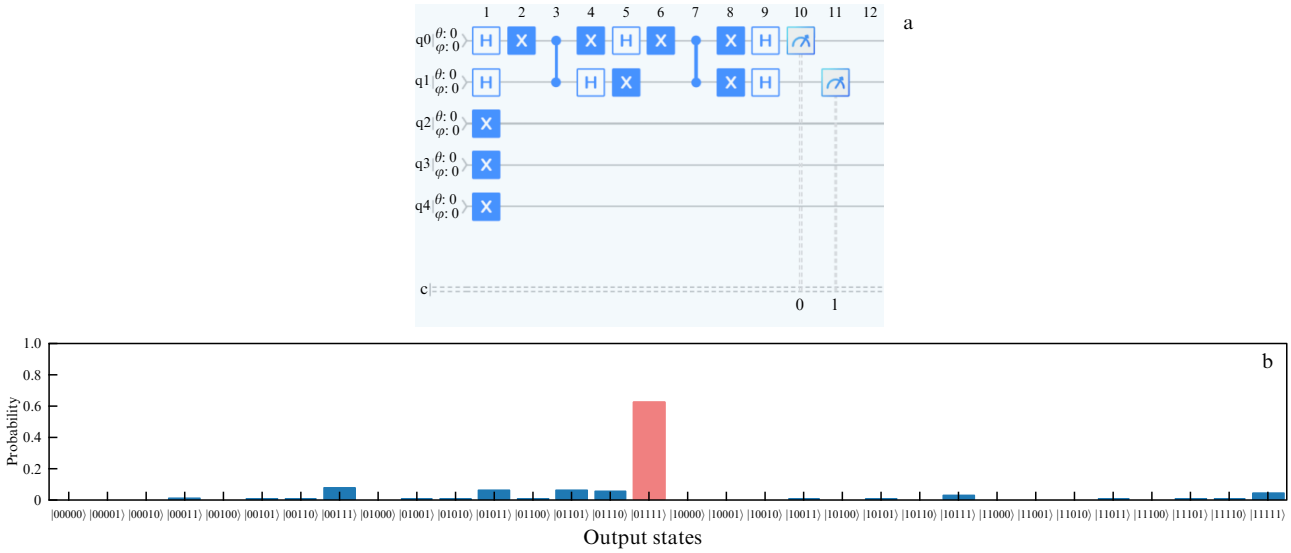

Figure 37. (a) A screenshot of cloud platform graphical editor used to prepare circuit corresponding to Grover's algorithm with key 01. (b) Results of executing the quantum circuit. Histogram is based on 1024 repetitions of the circuit. Expected output state is marked in red.

optimization algorithm (QAOA) was studied on the created computer. An example of such a circuit corresponding to a single QAOA layer is shown in Fig. 38a. Circuits and optimization problems of this type most effectively use the capabilities of the ion computer, because they require full connectivity and parameterized two-qubit and single-qubit operations (each two-qubit operation $ZZ(\chi_{ij})$ in the diagram is parameterized by its own rotation angle, which corresponds to a weighted problem). Figure 38b shows examples of comparing the expected distributions over the output states with those obtained experimentally for different numbers of ions involved (in all cases, there were 10 ions in the trap). The degree of agreement between the observed and expected distributions was determined using the formula from [10]:

$$F = \left(\sum_x \sqrt{P_{\text{ideal}}(x) P_{\text{meas}}(x)} \right)^2 .$$

Figure 38b shows that, as the problem size increases, the sampling accuracy decreases, as expected, which is due to the quadratic growth of the number of two-qubit operations (their total number is $n(n-1)/2$, where n is the number of qubits). Nevertheless, the histograms show that, for $n \leqslant 5$, the sampling accuracy remains quite high and reflects the main features of the distribution over output states. We used circuits of this type in an experiment on factoring the number 1591 into prime factors using the Schnorr algorithm [214].

Studies that actively use the qubit capabilities of the processor are of particular interest. One example of such studies is the simulation of the dynamics of a quantum system near the phase transition between PT-symmetric and PT-asymmetric Hamiltonians [73]. In that study, a method for simulating the dynamics of the simplest example of such a system using a qutrit was proposed. Importantly, the simulation of such a system requires at least two qubits, while the method proposed here allows this task to be accomplished using only one qutrit. This method was experimentally demonstrated using the created ion computer (the quantum register consisted of 10 ions; the calculations were performed in parallel on several particles simultaneously

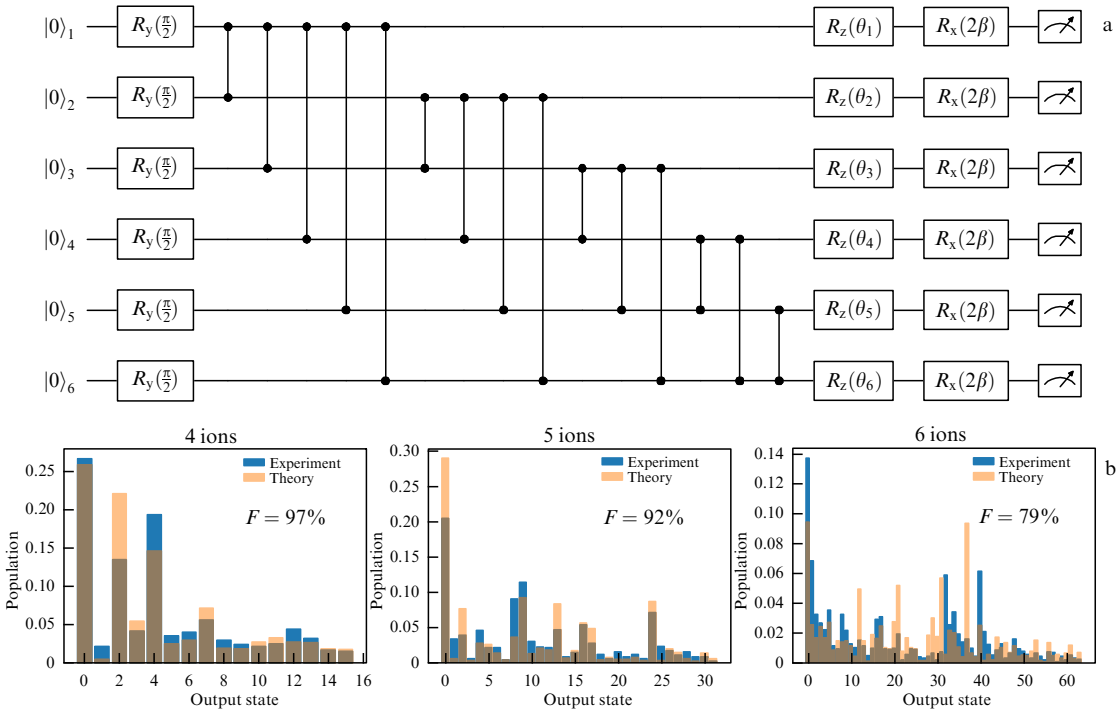

Figure 38. (a) Form of circuits used to characterize sampling accuracy on developed computer. Each circuit is parameterized by rotation angles θ_i and χ_{ij}, where χ_{ij} is phase of two-qubit operation $ZZ(\chi_{ij})$ between ions with numbers i and j (rotation angle is not indicated in diagram). (b) Examples of obtained histograms of output distributions for different numbers of ions involved. Theoretically predicted distributions are shown in blue, and experimentally obtained ones are shown in yellow. Results are averaged over 2000 circuit repetitions.

to speed up the collection of statistics) and a superconducting processor. The data obtained experimentally on both processors coincided with the theoretical calculation with high accuracy.

Another example showing the potential of using qudits to implement quantum algorithms is the concept of a scalable generalized Toffoli gate. The generalized Toffoli gate is understood here as an extension of that gate to more than three qubits. This gate is actively used in error correction, Grover's, and many other algorithms. Without using ancilla, the number of two-qubit operations involved in this gate scales quadratically, which greatly affects its fidelity. In [113, 114], a scheme for implementing this gate on ion computers was proposed with qubits replaced by qutrits. In this case, the third state is used as a pure ancilla. The number of two-qudit operations in this case depends linearly on the number of ions ($2N - 3$, where N is the number of ions affected by the gate), which means it can significantly improve the scaling of this operation. Using the created ion computer, this approach was demonstrated experimentally. The accuracies of the observed truth tables (output distributions after applying the gate to all possible states of the computation basis) were compared for the implementation of the gate using qubits and qutrits for $N = 3$–10 (in all cases, the full register consisted of 10 ions) [29]. For all N, the qudit approach was superior to the qubit one, and the advantage increased with increasing N. To demonstrate the phase properties of the resulting gate, Grover's algorithm with a Boolean oracle was implemented with it [29]. Its accuracy when using the Toffoli qudit gate also turned out to be higher than when using qubits.

6. Conclusions

Trapped ions are one of the first and most developed approaches to the implementation of quantum computers. Ion computers demonstrate record-breaking characteristics among all platforms in almost all indicators (fidelity of single-qubit and two-qubit operations, coherence time, connectivity, quantum volume) and are already used by third-parties via cloud access. Many studies are being conducted around the world aimed at developing these devices further.

One of the main focuses of this work is how to solve the problem of scaling: increasing the number of qubits without losing the fidelity of operations. The largest commercially available ion quantum computer today has 56 qubits [153] and is manufactured using QCCD technology. However, there are a number of promising studies and approaches aimed at further scaling and increasing the quality of qubits, including, for example, photonic interconnects [22, 215], fast nonadiabatic operations [194, 202], and laserless quantum gates [25, 216]. These and other methods will be described in more detail in our next review.

In this paper, we outlined the basic principles of operation of ion quantum computers and provided their basic characteristics. We also presented the main results achieved in this area in Russia within the Roadmap framework. Over the years, this field has developed in this country from a complete absence of ion computing technology to a full-fledged universal quantum computer with dozens of qubits and the development of an almost complete cycle of their construction, including laser and vacuum systems, as well as ion traps. In the course of the work, a number of new and promising ideas were implemented, the most striking of which is the

qudit architecture of processors, which made it possible to significantly increase the efficiency of devices. The achieved results open up broad opportunities both for the further development of the ion platform in Russia and for research in the field of quantum algorithms due to scientists' access to a real computing device.

Acknowledgments. We express our gratitude to A.K. Fedorov, A.S. Nikolaeva, E.O. Kiktenko, A.Yu. Chernyavsky, and B.I. Bantysh for assistance in algorithmic benchmarking of the quantum processor.

This work was supported by the Rosatom as part of the implementation of the Quantum Computing Roadmap (Agreement No. 868-1.3-15/15-2021 dated October 5, 2021).

References

1. The Nobel Prize in Physics 2012, https://www.nobelprize.org/prizes/physics/2012/summary/
2. DiVincenzo D P, in *Mesoscopic Electron Transport* (NATO ASI Ser. E, Vol. 345, Eds L L Sohn, L P Kouwenhoven, G Schön) (Dordrecht: Springer, 1997) p. 657, https://doi.org/10.1007/978-94-015-8839-3_18
3. Manin Yu I *Vychislimoe i Nevychislimoe* (Computable and Non-computable) (Moscow: Sov. Radio, 1980)
4. Benioff P *J. Stat. Phys.* **22** 563 (1980)
5. Feynman R P *Int. J. Theor. Phys.* **21** 467 (1982)
6. Moses S A et al. *Phys. Rev. X* **13** 041052 (2023)
7. Pogorelov I et al. *PRX Quantum* **2** 020343 (2021)
8. Abdurakhimov L "Technology and performance benchmarks of IQM's 20-qubit quantum computer," arXiv:2408.12433
9. Acharya R et al. (Google Quantum AI and Collab.) *Nature* **638** 920 (2025); arXiv:2408.13687
10. Chen J-S et al. "Benchmarking a trapped-ion quantum computer with 30 qubits," arXiv:2308.05071
11. IBM Quantum Platform (Accessed: 2024-10-15), https://quantum.ibm.com/ (IBM cloud platform)
12. Cirq. An open source framework for programming quantum computers (Accessed: 2024-10-15), https://quantumai.google/cirq (Google cloud platform cirq)
13. Microsoft Azure (Accessed: 2024-10-15), https://azure.microsoft.com (Azure Quantum cloud service)
14. Lidiruyushchii Issledovatel'skii Tsentr. Kvantovye Vychisleniya (Leading Research Center. Quantum Computing) (Accessed: 2024-10-15), https://qexplore-staging.lrc-quantum.ru (LRC cloud platform)
15. Cirac J I, Zoller P *Phys. Rev. Lett.* **74** 4091 (1995)
16. Leibfried D et al. *Rev. Mod. Phys.* **75** 281 (2003)
17. Paul W, Steinwedel H *Z. Naturforsch. A* **8** 448 (1953) https://doi.org/10.1515/zna-1953-0710
18. Penning F M *Physica* **3** 873 (1936)
19. Hänsch T W, Schawlow A L *Opt. Commun.* **13** 68 (1975)
20. Wang P et al. *Nat. Commun.* **12** 233 (2021)
21. Pino J M et al. *Nature* **592** 209 (2021)
22. Stephenson L J et al. *Phys. Rev. Lett.* **124** 110501 (2020)
23. Happer W *Rev. Mod. Phys.* **44** 169 (1972)
24. Harty T P et al. *Phys. Rev. Lett.* **113** 220501 (2014)
25. Löschnauer C M et al. "Scalable, high-fidelity all-electronic control of trapped-ion qubits," arXiv:2407.07694
26. Lekitsch B et al. *Sci. Adv.* **3** 1601540 (2017); arXiv:1508.00420
27. Sørensen A, Mølmer K *Phys. Rev. Lett.* **82** 1971 (1999); quant-ph/9810039
28. Baldwin C H et al. *Phys. Rev. A* **103** 012603 (2021)
29. Nikolaeva A S et al. "Scalable improvement of the generalized Toffoli gate realization using trapped-ion-based qutrits," arXiv:2407.07758
30. Fang C et al. "Realization of scalable Cirac-Zoller multi-qubit gates," arXiv:2301.07564
31. Turchette Q A et al. *Phys. Rev. Lett.* **81** 3631 (1998)
32. Schmidt-Kaler F et al. *Nature* **422** 408 (2003)
33. Monroe C et al. *Phys. Rev. Lett.* **75** 4011 (1995)
34. Turchette Q A et al. *Phys. Rev. A* **61** 063418 (2000); quant-ph/0002040
35. Lakhmanskiy K et al. *Phys. Rev. A* **99** 023405 (2019)
36. Blümel R et al. *Phys. Rev. A* **40** 808 (1989)
37. Benhelm J et al. *Phys. Rev. A* **77** 062306 (2008)
38. Greenberger D M, Horne M A, Zeilinger A "Going beyond Bell's theorem," in *Bell's Theorem, Quantum Theory and Conceptions of the Universe* (Fundamental Theories of Physics, Vol. 37, Ed. M Kafatos) (Dordrecht: Springer, 1989) p. 69, https://doi.org/10.1007/978-94-017-0849-4_10
39. Leibfried D et al. *Nature* **422** 412 (2003)
40. Leibfried D et al. *Science* **304** 1476 (2004)
41. Barrett M D et al. *Phys. Rev. A* **68** 042302 (2003); quant-ph/0307088
42. Schmidt P O et al. *Science* **309** 749 (2005)
43. Brewer S M et al. *Phys. Rev. Lett.* **123** 033201 (2019); arXiv:1902.07694
44. Micke P et al. *Nature* **578** 60 (2020)
45. Brickman K-A et al. *Phys. Rev. A* **72** 050306 (2005)
46. Blatt R, Roos C F *Nature Phys.* **8** 277 (2012); Johanning M, Varón A, Wunderlich C *J. Phys. B* **42** 154009 (2009); arXiv:0905.0118
47. Lanyon B P et al. *Science* **334** 57 (2011)
48. Monz T et al. *Phys. Rev. Lett.* **106** 130506 (2011)
49. Zhang J et al. *Nature* **551** 601 (2017)
50. Guo S-A et al. *Nature* **630** 613 (2024); arXiv:2311.17163
51. Zhu S-L, Monroe C, Duan L-M *Phys. Rev. Lett.* **97** 050505 (2006)
52. Choi T et al. *Phys. Rev. Lett.* **112** 190502 (2014)
53. Debnath S et al. *Nature* **536** 63 (2016); arXiv:1603.04512
54. Bluvstein D et al. *Nature* **626** 58 (2024)
55. Wineland D J et al. *J. Res. Natl. Inst. Stand. Technol.* **103** 259 (1998)
56. Kielpinski D, Monroe C, Wineland D J *Nature* **417** 709 (2002)
57. Lobser D L et al. "Precision control of ions in Sandia's HOA Trap," Technical Report SAND2019-11932C (Albuquerque, NM: Sandia National Lab., 2019)
58. Lobser D L et al. "Quantum and classical control of ions in Sandia's HOA Trap," Technical Report SAND2017-8584C (Albuquerque, NM: Sandia National Lab., 2017)
59. Moehring D L et al. *New J. Phys.* **13** 075018 (2011); arXiv:1105.1834
60. Shu G et al. *Phys. Rev. A* **89** 062308 (2014)
61. Maunz P L et al. "Ion traps for logical qubits," Technical Report SAND2017-1453C (Albuquerque, NM: Sandia National Lab., 2017)
62. Cross A W et al. *Phys. Rev. A* **100** 032328 (2019); arXiv:1811.12926
63. Aaronson S, Chen L "Complexity-theoretic foundations of quantum supremacy experiments," arXiv:1612.05903
64. Quantinuum extends its significant lead in quantum computing, achieving historic milestones for hardware fidelity and Quantum Volume, https://www.quantinuum.com/blog/quantinuum-extends-its-significant-lead-in-quantum-computing-achieving-historic-milestones-for-hardware-fidelity-and-quantum-volume
65. Zalivako I V et al. *Front. Quantum Sci. Technol.* **2** 1228208 (2023)
66. Zalivako I V et al. *Quantum Rep.* **7** (2) 19 (2025); arXiv:2402.03121
67. Zalivako I V et al. *JETP Lett.* **114** 59 (2021); *Pis'ma Zh. Eksp. Teor. Fiz.* **114** 53 (2021)
68. Zalivako I V et al. *Phys. Rev. A* **111** 052436 (2025); arXiv:2406.12007
69. Nikolaeva A S, Kiktenko E O, Fedorov A K *Phys. Rev. A* **109** 022615 (2024)
70. Podlesnyy A et al. "Parallel coupling of trapped ions in multiple individual wells," arXiv:2211.07121v1 (14 Nov. 2022); https://arxiv.org/pdf/2211.07121v1
71. Anikin E et al. *Phys. Rev. A* **108** 022402 (2023)
72. Aksenov M A et al. *Phys. Rev. A* **107** 052612 (2023)
73. Kazmina A S et al. *Phys. Rev. A* **109** 032619 (2024)
74. Floquet G *Ann. Sci. l'École Normale Supérieure 2* **12** 47 (1883) https://doi.org/10.24033/asens.220
75. Brouard S, Plata J *Phys. Rev. A* **63** 043402 (2001)
76. Dubin D H E *Phys. Rev. Lett.* **71** 2753 (1993)
77. Manning T A "Quantum information processing with trapped ion chains," PhD Thesis (College Park, MD: Univ. of Maryland, 2014); https://duke.app.box.com/s/7425eold3cfnodaklmec52xcp62kgtxs
78. James D F V *Appl. Phys. B* **66** 181 (1998)
79. Schmidt-Kaler F et al. *Appl. Phys. B* **77** 789 (2003)
80. Pagano G et al. *Quantum Sci. Technol.* **4** 014004 (2019)
81. Monroe C et al. *Phys. Rev. A* **89** 022317 (2014)

82. Rowe M A et al. *Quantum Inform. Comput.* **2** (4) 257 (2002) https://doi.org/10.26421/QIC2.4-1
83. Chiaverini J et al. *Quantum Inform. Comput.* **5** 419 (2005)
84. Seidelin S et al. *Phys. Rev. Lett.* **96** 253003 (2006)
85. House M G *Phys. Rev. A* **78** 033402 (2008)
86. Littich G "Electrostatic control and transport of ions on a planar trap for quantum information processing," Master's Thesis (Berkeley, CA: Univ. of California, 2011)
87. Kaushal V et al. *AVS Quantum Sci.* **2** 014101 (2020)
88. Kaufmann H et al. *Phys. Rev. A* **95** 052319 (2017)
89. Brownnutt M et al. *Rev. Mod. Phys.* **87** 1419 (2015)
90. Brown K R et al. *Nat. Rev. Mater.* **6** 892 (2021)
91. Romaszko Z D et al. *Nat. Rev. Phys.* **2** 285 (2020)
92. Bruzewicz C D et al. *Appl. Phys. Rev.* **6** 021314 (2019)
93. Revelle M C "Phoenix and peregrine ion traps," arXiv:2009.02398
94. Gerasin I et al. *Quantum Rep.* **6** 442 (2024)
95. Suleimen Y et al. *Phys. Rev. A* **109** 022605 (2024)
96. Abbasov T, Zibrov S, Sherstov I *JETP Lett.* **118** 215 (2023); *Pis'ma Zh. Eksp. Teor. Fiz.* **118** 212 (2023)
97. Ryan-Anderson C et al. *Phys. Rev. X* **11** 041058 (2021)
98. Ballance T G et al. *Rev. Sci. Instrum.* **89** 053102 (2018)
99. Leibrandt D R et al. *Phys. Rev. A* **76** 055403 (2007)
100. DeVoe R G, Kurtsiefer Ch *Phys. Rev. A* **65** 063407 (2002)
101. Daniilidis N et al. *New J. Phys.* **13** 013032 (2011)
102. Krutyanskiy V et al. *Phys. Rev. Lett.* **130** 050803 (2023)
103. Lucas D M et al. *Phys. Rev. A* **69** 012711 (2004)
104. Kjærgaard N et al. *Appl. Phys. B* **71** 207 (2000)
105. Gulde S et al. *Appl. Phys. B* **73** 861 (2001)
106. Wells J E et al. *Phys. Rev. A* **95** 053416 (2017)
107. Cetina M et al. *Phys. Rev. A* **76** 041401 (2007)
108. Lucas D M et al. "A long-lived memory qubit on a low-decoherence quantum bus," arXiv:0710.4421
109. Wright K et al. *Nat. Commun.* **10** 5464 (2019)
110. Leu A D et al. *Phys. Rev. Lett.* **131** 120601 (2023)
111. Nikolaeva A S, Kiktenko E O, Fedorov A K *EPJ Quantum Technol.* **11** 43 (2024)
112. Ralph T C, Resch K J, Gilchrist A *Phys. Rev. A* **75** 022313 (2007)
113. Nikolaeva A S, Kiktenko E O, Fedorov A K *Phys. Rev. A* **105** 032621 (2022)
114. Nikolaeva A S, Kiktenko E O, Fedorov A K *Entropy* **25** 387 (2023)
115. Low P J, White B, Senko C "Control and readout of a 13-level trapped ion qudit," arXiv:2306.03340
116. Ruster T et al. *Appl. Phys. B* **122** 254 (2016)
117. Blakestad R B et al. *Phys. Rev. A* **84** 032314 (2011)
118. Merkel B et al. *Rev. Sci. Instrum.* **90** 044702 (2019)
119. Viola L, Lloyd S *Phys. Rev. A* **58** 2733 (1998)
120. Valahu C H et al. *J. Phys. B* **55** 204003 (2022)
121. Ringbauer M et al. *Nat. Phys.* **18** 1053 (2022)
122. Olmschenk S et al. *Phys. Rev. A* **76** 052314 (2007)
123. Christensen J E et al. *npj Quantum Inform.* **6** 35 (2020)
124. An F A et al. *Phys. Rev. Lett.* **129** 130501 (2022)
125. Crain S et al. *Commun. Phys.* **2** 97 (2019)
126. Zalivako I V et al. *Quantum Electron.* **47** 426 (2017); *Kvantovaya Elektron.* **47** 426 (2017)
127. Koo K et al. *Phys. Rev. A* **69** 043402 (2004)
128. Sugiyama K *Jpn. J. Appl. Phys.* **38** 2141 (1999)
129. Goodwin J F et al. *Phys. Rev. Lett.* **116** 143002 (2016)
130. Han D-J et al. *Phys. Rev. Lett.* **85** 724 (2000)
131. Che H et al. *Phys. Rev. A* **96** 013417 (2017)
132. Sidorov P L et al. *Bull. Lebedev Phys. Inst.* **46** 138 (2019); *Kratk. Soobsch. Fiz. FIAN* (4)46 (2019)
133. Semenin N V et al. *JETP Lett.* **116** 77 (2022); *Pis'ma Zh. Eksp. Teor. Fiz.* **116** 74 (2022)
134. King B E et al. *Phys. Rev. Lett.* **81** 1525 (1998)
135. Roos Ch et al. *Phys. Rev. Lett.* **83** 4713 (1999)
136. Letchumanan V et al. *Phys. Rev. A* **75** 063425 (2007)
137. Chen J-S et al. *Phys. Rev. A* **102** 043110 (2020)
138. Lechner R et al. *Phys. Rev. A* **93** 053401 (2016)
139. Zhang J et al. *Phys. Rev. Applied* **18** 014022 (2022)
140. Lin Y et al. *Phys. Rev. Lett.* **110** 153002 (2013)
141. Jordan E et al. *Phys. Rev. Lett* **122** 053603 (2019)
142. Semerikov I A et al. *J. Russ. Laser Res.* **39** 568 (2018)
143. Feng L et al. *Phys. Rev. Lett.* **125** 053001 (2020)
144. Mao Z-C et al. *Phys. Rev. Lett.* **127** 143201 (2021)
145. Wübbena J B et al. *Phys. Rev. A* **85** 043412 (2012)
146. Barrett M D et al. *Phys. Rev. A* **68** 042302 (2003)
147. Yum D et al. *J. Korean Phys. Soc.* **77** 1143 (2020)
148. Tanaka U et al. *Appl. Phys. B* **121** 147 (2015)
149. Cui K et al. *J. Phys. B* **51** 045502 (2018)
150. Todaro S L et al. *Phys. Rev. Lett.* **126** 010501 (2021)
151. Semenin N V et al. *JETP Lett.* **114** 486 (2021); *Pis'ma Zh. Eksp. Teor. Fiz.* **114** 553 (2021)
152. Chen J-S et al. *Quantum* **8** 1516 (2024)
153. Quantinuum System Model H2. Product Data Sheet, Version 2.00, October 15, 2024, https://docs.quantinuum.com/systems/data_sheets/Quantinuum%20H2%20Product%20Data%20Sheet.pdf
154. Myerson A H et al. *Phys. Rev. Lett.* **100** 200502 (2008); arXiv:0802.1684
155. Hampel B et al. *Appl. Phys. Lett.* **122** 174001 (2023)
156. Nielsen M A, Chuang I L *Quantum Computation and Quantum Information* (Cambridge: Cambridge Univ. Press, 2010) https://doi.org/10.1017/CBO9780511976667
157. Srinivas R et al. *Nature* **597** 209 (2021)
158. Johanning M et al. *Phys. Rev. Lett.* **102** 073004 (2009)
159. Abdel-Hafiz M et al. "Guidelines for developing optical clocks with 10^{-18} fractional frequency uncertainty," arXiv:1906.11495
160. Lee P J et al. *J. Opt. B* **7** (10) S371 (2005) https://doi.org/ 10.1088/1464-4266/7/10/025
161. McKay D C et al. *Phys. Rev. A* **96** 022330 (2017)
162. Hrmo P et al. *Nat. Commun.* **14** 2242 (2023)
163. Riebe M et al. *Phys. Rev. Lett.* **97** 220407 (2006)
164. Mohseni M, Rezakhani A T, Lidar D A *Phys. Rev. A* **77** 032322 (2008)
165. Knill E et al. *Phys. Rev. A* **77** 012307 (2008)
166. Arute F et al. *Nature* **574** 505 (2019)
167. Greenbaum D "Introduction to quantum gate set tomography," arXiv:1509.02921
168. Campbell W C et al. *Phys. Rev. Lett.* **105** 090502 (2010)
169. Smith M C et al. *Phys. Rev. Lett.* **134** 230601 (2025); arXiv:2412.04421
170. Bermudez A et al. *Phys. Rev. X* **7** 041061 (2017)
171. Ballance C J et al. *Phys. Rev. Lett.* **117** 060504 (2016)
172. Gaebler J P et al. *Phys. Rev. Lett.* **117** 060505 (2016)
173. Keselman A et al. *New J. Phys.* **13** 073027 (2011)
174. Ospelkaus C et al. *Nature* **476** 181 (2011)
175. Shappert C M et al. *New J. Phys.* **15** 083053 (2013)
176. Brown K R et al. *Phys. Rev. A* **84** 030303 (2011)
177. Hahn E L *Phys. Rev.* **80** 580 (1950)
178. Roos C F *New J. Phys.* **10** 013002 (2008)
179. Wimperis S *J. Magn. Reson. A* **109** 221 (1994)
180. Brown K R, Harrow A W, Chuang I L *Phys. Rev. A* **70** 052318 (2004)
181. Low G H, Yoder T J, Chuang I L *Phys. Rev. A* **89** 022341 (2014)
182. Cummins H K, Llewellyn G, Jones J A *Phys. Rev. A* **67** 042308 (2003)
183. Bando M et al. *J. Phys. Soc. Jpn.* **82** 014004 (2013)
184. Kabytayev C et al. *Phys. Rev. A* **90** 012316 (2014)
185. Paz-Silva G A, Viola L *Phys. Rev. Lett.* **113** 250501 (2014)
186. Ball H, Biercuk M J *EPJ Quantum Technol.* **2** 11 (2015)
187. Mount E et al. *Phys. Rev. A* **92** 060301 (2015)
188. Soare A et al. *Nature Phys.* **105** 825 (2014)
189. DiVincenzo D P *Fortschr. Phys.* **48** 771 (2000)
190. Diedrich F et al. *Phys. Rev. Lett.* **62** 403 (1989)
191. Morigi G, Eschner J, Keitel C H *Phys. Rev. Lett.* **85** 4458 (2000)
192. Evers J, Keitel C H *Europhys. Lett.* **68** 370 (2004)
193. Kranzl F et al. *Phys. Rev. A* **105** 052426 (2022)
194. Wang K et al. *Quantum Sci. Technol.* **7** 044005 (2022)
195. Gunton W, Semczuk M, Madison K M *Opt. Lett.* **40** 4372 (2015)
196. Aolita L et al. *Phys. Rev. A* **76** 040303 (2007)
197. Blinov B B et al. *Quantum Inform. Process.* **3** 45 (2004)
198. Sackett C A et al. *Nature* **404** 256 (2000)
199. IonQ Forte, https://ionq.com/quantum-systems/forte
200. Erhard A et al. *Nat. Commun.* **10** 5347 (2019)
201. Zhang S et al. *Nat. Commun.* **11** 587 (2020)
202. Schäfer V M et al. *Nature* **555** 75 (2018)
203. Hughes A C et al. *Phys. Rev. Lett.* **125** 080504 (2020)

204. Clark C R et al. *Phys. Rev. Lett.* **127** 130505 (2021)
205. Johnson K G et al. *Rev. Sci. Instrum.* **87** 053110 (2016)
206. Berkeland D J, Boshier M G *Phys. Rev. A* **65** 033413 (2002)
207. Zalivako I V et al. *Quantum Electron.* **50** 850 (2020); *Kvantovaya Elektron.* **50** 850 (2020)
208. Galstyan K P, Zalivako I V, Kryuchkov D S, Kolachevsky N N *Radiophys. Quantum Electron.* **67** 13 (2024); *Izv. Vyssh. Uchebn. Zaved. Radiofiz.* **67** (1) 15 (2024)
209. Benhelm J et al. *Nature Phys.* **4** 463 (2008)
210. Bharti K, Haug T *Phys. Rev. A* **104** L050401 (2021)
211. Bharti K, Haug T *Phys. Rev. A* **104** 042418 (2021)
212. Haug T, Bharti K *Quantum Sci. Technol.* **7** 045019 (2022)
213. Bharti K et al. *Phys. Rev. A* **105** 052445 (2022)
214. Zalivako I V et al. ''Experimental factoring integers using fixed-point-QAOA with a trapped-ion quantum processor,'' arXiv:2503.10588
215. Main D et al. *Nature* **638** 383 (2025); arXiv:2407.00835
216. Mintert F, Wunderlich C *Phys. Rev. Lett.* **87** 257904 (2001)